Department of Physics and Astronomy

University of Heidelberg

Master Thesis in Physics

submitted by

Kristian Rink

born in Göttingen, Germany

2012

Spectral Computed Tomography at High Photon Fluxes

This master thesis has been carried out by Kristian Rink at the
German Cancer Research Center (DKFZ) in Heidelberg
under the supervision of
Prof. Dr. Uwe Oelfke and
Prof. Dr. Wolfgang Schlegel

Abstract

The development of pixelated photon counting semiconductor detectors enables to resolve the spectral composition of the incident photons in X-ray imaging, provided that the detector is operated in the absence of pulse pile-up and sensor polarisation. The purpose of this study is to examine the imaging properties of Medipix2 MXR detectors under high photon fluxes, which do not meet this requirement.

At first, it is shown that the critical photon flux, at which the detector's linearity breaks down, can be shifted towards higher values by increasing the I_{Krum} current in the charge sensitive preamplifier, which corresponds to reducing the pulse shaping time. The negative impact of this procedure on the detector's spectroscopic performance seems only moderate.

Furthermore, the deviation from an ideal linear response is determined as a function of the photon flux. The deviations are used to correct single projections and eventually acquire spectral CT images at high photon fluxes which contain corrected absorption coefficients. Thus, K-edge imaging with the contrast agents iodine and gadolinium can be performed at high photon fluxes. It is shown that the spectroscopic information vanishes for energy ranges, which correspond to energies higher than approximately the mean photon energy of the incident spectrum.

Kurzfassung

Die Entwicklung von pixelierten, photonenzählenden Halbleiterdetektoren ermöglicht, die spektrale Zusammensetzung der eintreffenden Photonen bei der Röntgenbildgebung aufzulösen. Allerdings treten bei erhöhten Photonenflüssen Nebeneffekte wie Puls Pile-up und Sensor-Polarisation stark in Erscheinung und müssen weitestgehend ausgeblendet werden. Um diese notwendigen Voraussetzungen zu realisieren, werden in der vorliegenden Arbeit die Eigenschaften von Medipix2 MXR Detektoren bei hohen Photonenflüssen untersucht.

Zunächst wird gezeigt, dass der kritische Photonenfluss, bei dem die Detektorlinearität abbricht, zu höheren Werten hin angehoben werden kann, wenn der Entladestrom I_{Krum} des Vorverstärkers erhöht wird. Dies bedeutet eine Verkürzung der Zeit, in der im Vorverstärker Ladungen in Spannungspulse gewandelt werden. Negative Auswirkungen dieses Verfahrens auf die spektroskopische Leistungsfähigkeit des Detektors erscheinen hier nur geringfügig.

Weiterhin wird die Abweichung von der idealen, linearen Reaktion als eine Funktion des Photonenflusses bestimmt. Diese Abweichungen werden verwendet, um einzelne Projektionen zu korrigieren und um schließlich spektrale CT Bilder bei hohen Photonenflüssen aufzunehmen, die berichtigte Absorptionskoeffizienten enthalten. Deswegen kann die K-Kanten-Bildgebung der Kontrastmittel Iod und Gadolinium bei hohen Photonenflüssen durchgeführt werden. Es wird gezeigt, dass die spektroskopische Information verloren geht für Energiefenster, die höheren Energien entsprechen als etwa die mittlere Photonenenergie des einfallenden Spektrums.

Publications

Parts of this master thesis were presented on a poster at the „14th international Workshop on Radiation Imaging Detectors" (iWoRID 2012) in Figueira da Foz (Portugal). Furthermore, the following two research articles contain results that were obtained in this work:

- K. Rink, T. Koenig, M. Zuber, A. Zwerger, A. Fauler, M. Fiederle and U. Oelfke [2012], 'Saturation Effects of CdTe Photon Counting Detectors Under High Photon Fluxes', *J. Inst.*, **accepted**.

- T. Koenig, J. Schulze, M. Zuber, K. Rink, J. Butzer, E. Hamann, A. Cecilia, A. Zwerger, A. Fauler, M. Fiederle and U. Oelfke [2012], 'Imaging properties of small-pixel spectroscopic X-ray detectors based on cadmium telluride sensors', *Phys. Med. Biol.* **57**, 6743-6759.

Contents

1 Introduction & Motivation

One of the greatest achievements in medical physics was computed tomography (CT), which was invented in the 1970s, and for which the Nobel Prize was awarded to Allan M. Cormack and Godfrey N. Hounsfield in 1979. This technique was revolutionary since it enables to produce cross-sectional images for diagnostic and therapeutic purposes. Until today, CT belongs to the most important imaging modalities in cancer diagnostics. Although a patient examined by CT is exposed a radiation dose, CT cannot be replaced by any other non-invasive 3D imaging technique, such as magnetic resonance imaging (MRI). The main advantages of CT are high spatial resolution, fast image acquisition times and a good contrast between soft tissues and bones. Nevertheless, the soft tissue contrast in CT images can be inferior to MRI [Schlegel and Bille, 2002].

Conventional CT images do not feature a spectral resolution, i.e. information about the wavelength or energy of the detected photons. This is made possible with spectral CT, in which the diagnostic opportunities are increased. But the future of spectral imaging techniques is closely connected to the development of energy resolving detectors [Koenig, 2011 a; Schlomka et al., 2008; Shikhaliev, 2008; Shikhaliev and Fritz, 2011].
Recently, the research of technologies in the field of particle detection at the European Organisation for Nuclear Research (CERN) in Geneva also lead to the development of the so-called Medipix detectors. These photon counting X-ray detectors are able to discriminate between photon energies and consequently distinguish between different elements with similar absorption coefficients using spectral information. Furthermore, images can be taken that do not exhibit a dark current and are consequently free of noise. However, a common drawback of these detectors is their susceptibility to pulse pile-up and sensor polarisation under high photon fluxes. In medical CT, photon fluxes as high as $10^9 \, \mathrm{mm}^{-2} \, \mathrm{s}^{-1}$ are required to avoid motion blur and in order to maintain a high photon throughput across a patient. Yet, state-of-the-art photon counting detectors provide maximum count rates orders of magnitudes smaller than this requirement [Koenig et al., 2012].

The purpose of this master thesis is to study the count rate limitations of Medipix2 MXR detectors operated with cadmium telluride (CdTe) sensors. An algorithm is developed, which corrects the measured photon flux for each pixel of the detector chip, when the detector's linearity breaks down. In this manner, it should be possible to record spectral CT images with corrected absorption coefficients and in an efficient acquisition time. This correction method is limited by the mean energy of the incident spectrum.

The following topics will be covered in the upcoming chapters:

- **What happens at high photon fluxes (chapter 4.3)?**

  Photon counting systems do not exhibit a perfectly linear dynamic range at high photon fluxes. Instead, two different types of saturation effects can occur, which influence this desired behaviour. Pulse pile-up denotes the phenomenon of overlapping signals in the detector electronics. Sensor polarisation happens when trapped charges accumulate in the sensor and counteract the applied internal electric field. As a consequence, charges need more time to reach the electrodes and may be subject to increased trapping. Therefore, both spectroscopic performance as well as imaging quality are reduced and the acquisition time is increased.

- **Which effects occur when the detector settings are adjusted (chapter 4.4)?**

  It will be studied how the detectors employed in this work have to be operated in order to minimise pile-up and / or polarisation by changing the preferences of several digital-to-analog converters (DAC) in the detector electronics and which impact they have on a detector's spectroscopic performance. Additionally, several detector artefacts, which degrade the image quality and which depend on the detector configurations, are analysed.

- **Is it possible to correct saturation effects in the resulting images (chapter 4.6)?**

  Each pixel has its own characteristics and therefore behaves in a different way. Hence, detector settings might be adjusted and an algorithm has to be developed to compensate this undesired behaviour. Since all photon counting detectors are affected by pulse pile-up and sensor polarisation, the correction method should be transferable to upcoming detector developments.

Before these questions are investigated, the fundamental physics governing these detectors will be discussed in chapter 2. Chapter 3 will describe the experimental setup used and give the basics for CT image reconstruction.

2 Theory

In this chapter, the required basics for the understanding of this master thesis are presented. Initially, X-radiation in general is outlined, followed by the physics of semiconductors and detection principles. Also the history of the Medipix detector family is summarised.

2.1 X-Radiation

X-rays are one of the fundamentals of medical physics, especially of medical imaging. They are a form of electromagnetic radiation with wavelength of 10^{-9} to 10^{-11} m, corresponding to photons in the energy range of several keV. There are two possible ways to generate X-rays: Either they can be produced by decelerating an electrically charged particle, which is called *bremsstrahlung*, or in terms of *characteristic X-rays* by electric transitions in excited atoms, as illustrated in figure 2.1. Whereas bremsstrahlung is characterised by a continuous spectrum, characteristic X-rays, as the name indicates, feature discrete energy peaks depending on the element by which they are generated.

a) generation of bremsstrahlung   b) generation of a characteristic photon
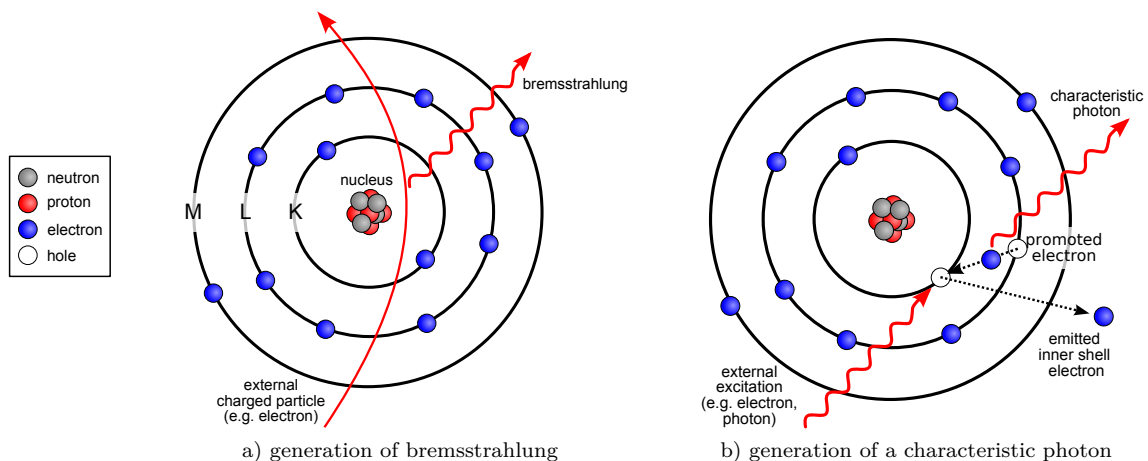
Figure 2.1: Different processes in an atom to generate X-rays. Whereas on the left the energy of the photon can vary depending on the deceleration of the charged particle, the energy of the photon on the right is discrete.

In the shell model, an atom consists of a dense positively charged core called nucleus, which is composed of protons and neutrons and is surrounded by various

shells, which are filled with electrons. The number of these shells depends on the element. The shell closest to the nucleus is named K, whereas the outer shells are named by the succeeding letters of the alphabet [Schlegel and Bille, 2002].

The characteristic radiation of an atom can be illustrated in an atomic relaxation model. An example is shown in figure 2.2. In this model, a specific photon energy and hence a specific frequency corresponds to each transition between two different atomic shells. These transitions can be observed as well-defined peaks in X-ray spectrometry, which is used to identify the composition of elements of a certain material. From atomic physics it is known, that the transitions are limited by the selection rules. The notation on the left contains principal, angular momentum and spin quantum numbers. The letters on the right refer to the different states in an atom. The Greek letters and numbers after the transition arrows correspond to the *Siegbahn notation*, which is used to label the various transitions according to their intensities [Salvat et al., 2001]. The characteristic X-ray peaks for tungsten (W) with the highest intensities are listed in table 2.1.
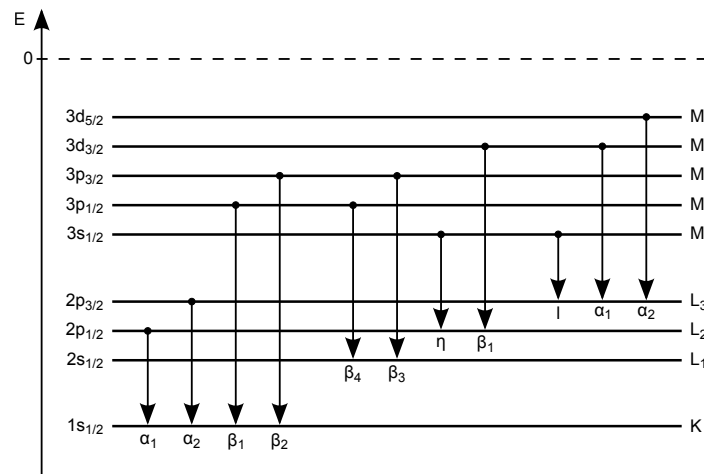
Figure 2.2: Schematic model of atomic relaxations and its corresponding nomenclature, adopted from Salvat et al. [2001]. The notation on the left qualifies the different quantum numbers. The Greek letters and numbers behind the transition arrows correspond to the Siegbahn notation.

2.1.1 X-Ray Tubes

A typical way to produce X-rays in the laboratory is by using an X-ray tube, which is illustrated schematically in figure 2.3. In an evacuated tube, electrons are emitted by a thermionic cathode, which is heated by the cathode voltage U_c. Afterwards, the electrons are accelerated towards the anode by the anode voltage U_a. When the electrons are scattered at the anode they release their kinetic energy in terms of radiation and heat. Since the latter effect dominates, the anode has to be cooled

	energy [keV]	relative intensity
$K_{\alpha2}$	58,0	0.25
$K_{\alpha1}$	59,3	0.50
$K_{\beta1}$	67,2	0.17
$K_{\beta2}$	69,1	0.07

Table 2.1: Major characteristic X-ray peaks for tungsten[1]. Compared to figure 2.2, the energy levels $2p_{1/2}$ and $2p_{3/2}$ for tungsten are degenerated reversely, which leads to $E_{K\alpha1} > E_{K\alpha2}$.

depending on the electrical power. Only a fraction of the generated radiation escapes from the tube through an X-ray transparent window[Mertins and Gilbert, 2006].
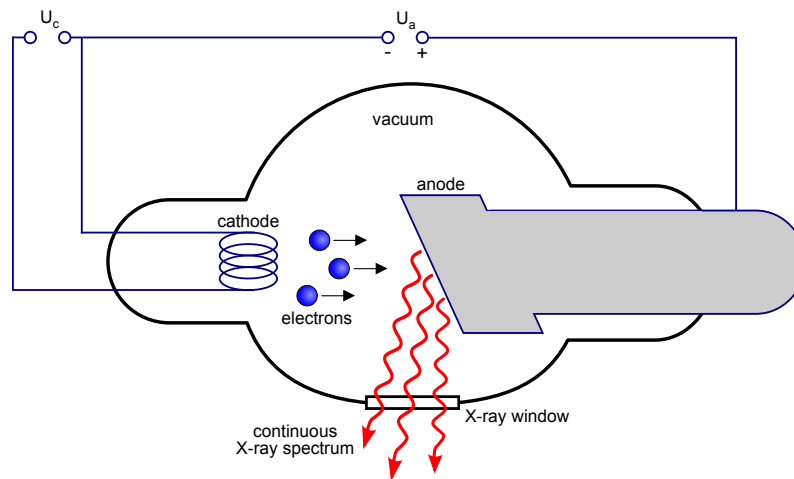
Figure 2.3: Schematic setup of an X-ray tube. The electrons produce bremsstrahlung and characteristic X-rays as well as heat when they are scattered at the anode.

2.1.2 Interaction of X-Rays with Matter

X-rays have the property to penetrate matter but lose intensity due to several effects. For monochromatic radiation this behaviour is described by the *Lambert-Beer Law*. The intensity of the outgoing radiation $N(\mu, \Delta x)$ can be calculated by equation 2.1, where N_0 denotes the initial intensity, μ the absorption coefficient and Δx the thickness of the irradiated material (see also figure 3.11a). Furthermore, μ depends on the photon energy E_γ and the atomic number Z [Schlegel and Bille, 2002].

$$N = N_0 \, e^{-\mu(E_\gamma, Z) \cdot \Delta x} \tag{2.1}$$

---

[1] characteristic X-ray peaks obtained from the National Physical Laboratory (NPL), Kaye & Laby, tables of physical & chemical constants [Online; accessed 20-October-2012]:
http://www.kayelaby.npl.co.uk/atomic_and_nuclear_physics/4_2/4_2_1.html

Photons can interact with matter by several processes depending on their energy. Illustrated in figure 2.4, these are the *photoelectric effect*, the *Compton effect* (incoherent / inelastic scattering) and *Thomson scattering* (coherent / elastic scattering).

(a) photoelectric effect **(b)** Compton effect **(c)** Thomson scattering
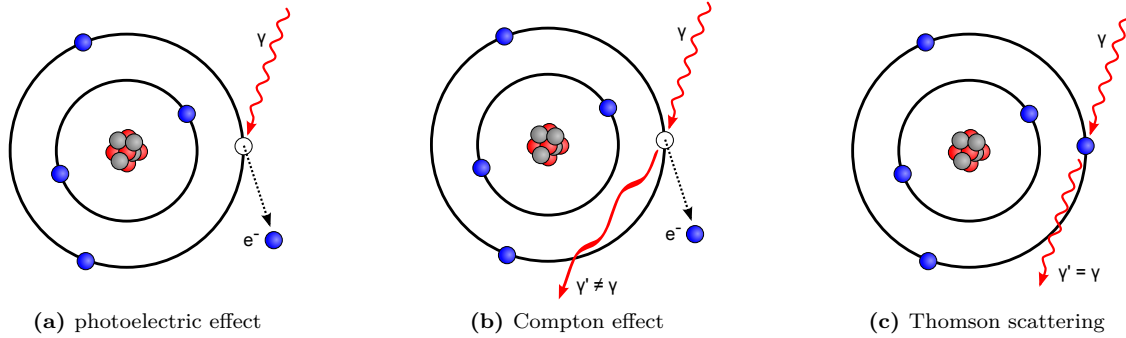
Figure 2.4: The most important interactions of X-rays with matter.

Photoelectric absorption happens when an electron, which is part of an atom, is ejected from its shell after an interaction with a photon. The energy of the incoming photon has to be at least as high as the binding energy of the electron. The remaining photon energy is transformed into kinetic energy of the electron and the photon vanishes. The Compton effect is known as an incoherent scattering of a photon at an electron of an outer atomic shell without being absorbed completely. This scattering leads to a free electron and a secondary photon with a different wavelength. In Thomson scattering the incoming photon scatters elastically with an atomic electron. Thereby, the photon as well as the electron keep their energy but change their phase. Hence, the total absorption coefficient is divided into parameters of the three mentioned interactions in equation 2.2. Here, $F(E_\gamma, Z)$ indicates a form factor and $3 \leq a \leq 4$ with $a \in \mathbb{R}$ [Kane et al., 1986].

$$\mu = \mu_{photo} + \mu_{Compton} + \mu_{Thomson} \tag{2.2}$$

$$\text{with} \quad \mu_{photo} \sim Z^a E_\gamma^{-3}$$
$$\mu_{Compton} \sim Z E_\gamma^{-1}$$
$$\mu_{Thomson} \sim F^2(E_\gamma, Z)$$

In figure 2.5, an example of the attenuation coefficients for tungsten is given. The three peaks in the photoelectric effect curve at around 2, 12 and 69 keV indicate the M, L and K-edges, which have already been mentioned in section 2.1. The reason for these steps is that more energy is needed to release an electron from an inner shell than from an outer one. This translates into an increase of the absorption coefficient when the photon energy is large enough to detach an electron from the next shell.

Another important aspect of this figure is that for low photon energies around 100 keV as used in conventional CT, photoelectric absorption mainly determines the absorption coefficient. This fact is enhanced by $\mu_{photo} \sim E_{\gamma}^{-3}$ (see the legend of equation 2.2). Note that elements featuring low atomic numbers can be severely influenced by Compton scattering.
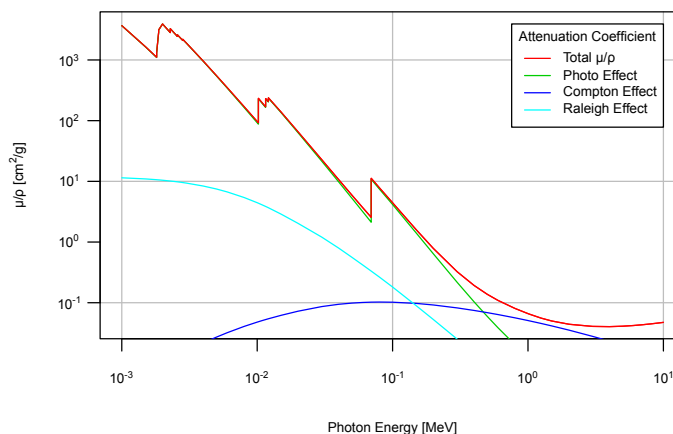
Figure 2.5: Illustration of the attenuation coefficient for tungsten in double logarithmic scale[2]. The three steps in the photo effect curve correspond to the M, L and K-edges originated from the different atomic shells.

2.1.3 X-Ray Detection Systems

There are different ways to convert X-rays into digital signals, as illustrated in figure 2.6: *Direct photon detection systems* convert X-rays to electrical charges in the sensor itself. Therefor the sensor has to consist of a semiconductor material in which the incoming X-rays produce electron-hole pairs. These charges are carried to the electrodes by a high bias voltage. The electrical output signal, which can be processed further, is gained by a transistor array in an active matrix readout. Therefor the charges obtained in the semiconductor are collected separately for each pixel. *Indirect systems* typically use scintillators to convert X-rays into visible light. Scintillators are luminescent materials, which are used as intermediate layers. Afterwards, the visible light is converted into an electric charge either by using a photodiode combined with a transistor array or by using a charge-coupled device (CCD). CCD imaging sensors consist of a photodiode array, which establishes the pixel matrix. Advantages of transistor arrays compared to CCDs are a shortened readout time and the possiblity to build up larger photosensitive areas. However, indirect detection systems lead to a reduction of contrast and spatial as well as energy resolution due

---

[2]mass attenuation coefficients obtained from the National Institute of Standards and Technology (NIST), XCOM: photon cross sections database [Online; accessed 20-October-2012]: `http://www.nist.gov/pml/data/xcom/index.cfm`

to more diffusion [Antonuk et al., 2000].
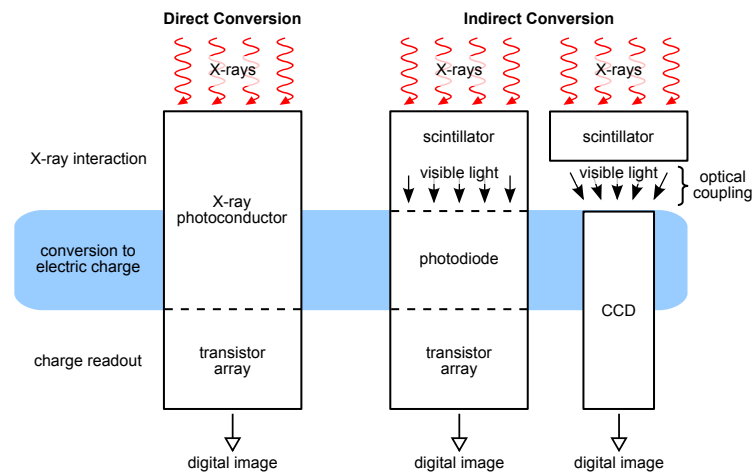
Figure 2.6: X-ray conversion for electronically readable detectors.

The processing of the detected signal can also be done in different ways: In case of an *energy integrating system* the collected current pulses produced by detected X-rays are added up without any further treatment. But also electrical currents originated from other sources than the detected signals are summed up. These are e. g. detector leakage currents, which contribute noise to the accumulated signals. When a photon is completely absorbed in the sensor, the number of generated charges is directly proportional to its energy. The image contrast in X-ray projections is gained by the absorption of photons in different objects. So, low energy photons transmitted through an object are more attenuated and hence, they carry more information than high energy photons. But by weighting the photon by its energy, as energy integrating systems do, the image contrast carried by low energy photons is weighted less and the Poisson noise contribution from high energy photons is increased. This results in a decrease of the signal-to-noise ratio (SNR).

A contrary method is given with a *photon counting system.* Here, the collected charges are converted to a voltage signal which is compared to a threshold. If the signal exceeds the threshold, a counter will be incremented. In this way, the contribution of detector leakage currents is removed by the threshold so that also low flux rate imaging can be performed. Furthermore, in photon counting systems photons are equally weighted independent on their energy since only the validity of an event is registered. Another remarkable advantage of a threshold is the possibility to remove not only noise from the signal but also to discriminate different photon energies [Llopart, 2007].

2.2 The Principle of Semiconductor Detectors

Semiconductors are solid state objects with an electrical conductivity $\sigma = \frac{1}{R}$, intermediate to that of conductors and insulators. So, it is the inverse of resistivity

R. The conductivity quantifies how strongly a material opposes the flow of electric current and is defined in equation 2.3. Here, e describes the elementary charge, n_i the density of the charge carriers and μ_i the mobility. The negative charge carriers are labeled with an index e for electrons and h for holes:

$$\sigma = e\left(n_e \mu_e + n_h \mu_h\right). \tag{2.3}$$

The conductivity can be described in a model of different band structures, as illustrated in figure 2.7. The bands are filled with electrons depending on their energy levels. At a temperature of $T = 0\,K$, the energetically highest band that is completely filled with electrons is named valence band. It is separated to the next higher band, which is called conduction band, by a band gap E_g. Insulators have a wide band gap between valence and conduction band. Additionally, the valence band is full of electrons, whereas the conduction band is empty. These two reasons lead to the fact that in an insulator the internal electric charge cannot flow freely. In contrast, in a conductor the two bands are overlapping so that the conductor band is partly filled and the electrons can move freely. At $T = 0\,K$, semiconductors behave like insulators since the electrons are not able to reach the conduction band although their band gap is smaller than in an insulator. But when the electrons are excited it may be possible for them to reach the conduction band. Consequently, then they leave holes in the valence band, which can be considered as positive charges.
The Fermi energy E_F at $T = 0\,K$ indicates the ground level at which every state is occupied below E_F [Hunklinger, 2009].
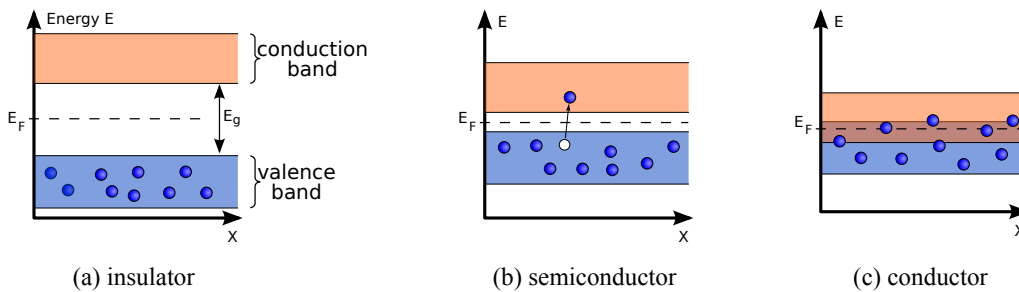
Figure 2.7: Comparison of insulators, semiconductors and conductors. Whereas also for $T > 0\,K$ in an insulator E_g is too large for the electrons to reach the conduction band, in a conductor this gap does not exist. At $T = 0\,K$, a semiconductor behaves as an insulator, but at higher temperatures or through ionising radiation the creation of electron-hole pairs is possible [Hunklinger, 2009].

2.2.1 Semiconductor Junctions

To increase the conductivity of *intrinsic semiconductors*, which are pure materials, it is possible to dope them with elements featuring a different number of free charge carriers. This means that single atoms from the semiconductor crystal are replaced by either *donors*, which bring along free electrons, or *acceptors*, which bring along

free holes. Here, the former is called n-type doping, the latter p-type doping. Several junctions are important to construct and connect electrical circuits to semiconductor components. A *pn-junction* is formed at the boundary between a p-type and an n-type doped material in a single compound structure. Figure 2.8 illustrates how E_F is balanced within the whole semiconductor in the thermodynamic equilibrium, which is achieved by diffusion between the doped materials.

(a) p- and n-doped semiconductors   (b) pn-junction
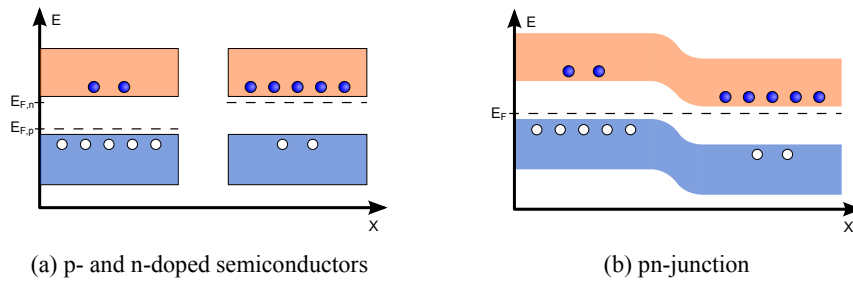
Figure 2.8: Sketch of a pn-junction. While the p- and n-doped materials on the left are separated, on the right, the charge carriers are able to move through the mutual band structure [Hunklinger, 2009].

Another type of junction can be constructed by combining a conductor with a semiconductor. As in a pn-junction, adjoining these two materials results in an adjustment of E_F, which is illustrated for an n-doped semiconductor in figure 2.9.

(a) ohmic contact
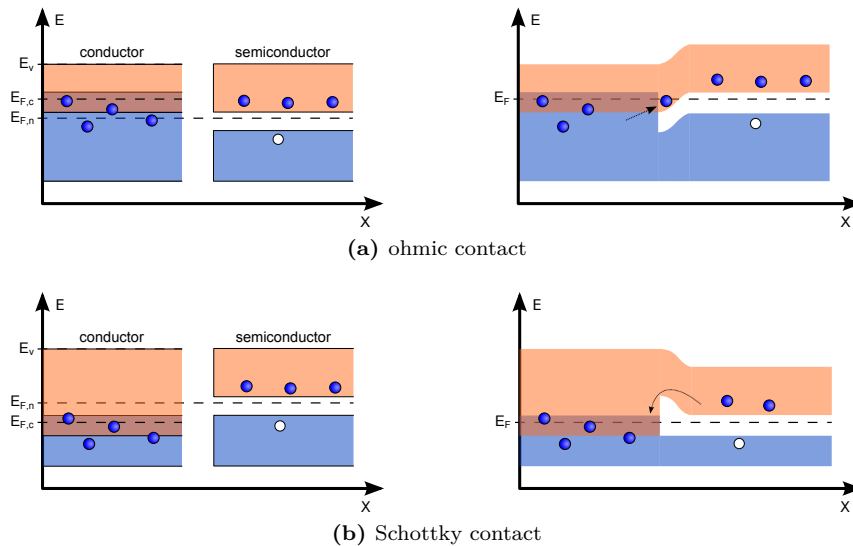
(b) Schottky contact

Figure 2.9: Illustration of the processes occuring when a conductor is connected with a semiconductor material. While in an ohmic contact electrons will flow from the conductor to the semiconductor, in a Schottky contact they attempt to overcome the barrier to flow to the conductor [Hunklinger, 2009].

The conductor-semiconductor junction is called *ohmic contact* when $E_{F,c}$ of the conductor is higher than $E_{F,n}$ of the n-doped semiconductor. In order to be balanced, electrons will flow from the metal to the semiconductor, which leads to a bending of the conduction band. This effect is strong enough to move the conduction band below E_F at the contact layer so that there are many free charges. Hence, if an external voltage is applied, the electrons will flow through the junction.

In contrast to an ohmic contact, the metal-semiconductor junction is called *Schottky contact*, if $E_{F,c}$ is lower than $E_{F,n}$. In this case the electrons will flow from the semiconductor into the metal, which leads to a depletion layer at the interface. Consequently, a potential barrier named *Schottky barrier* is formed [Hunklinger, 2009].

2.2.2 Semiconductor Detectors

The fundamental principle of a semiconductor detector including the signal curves after the individual components is shown in figure 2.10. The incident radiation is absorbed in a semiconductor sensor and due to a high bias voltage introduced to a charge sensitive preamplifier, whose output voltage is proportional to the charges Q at its input. Subsequently, the voltage pulse U is fed into a pulse shaper and then digitised for further analysis in an analog-to-digital converter (ADC) [Spieler, 2006]. The function of the pulse shaping device is explained in more detail in figure 2.11.
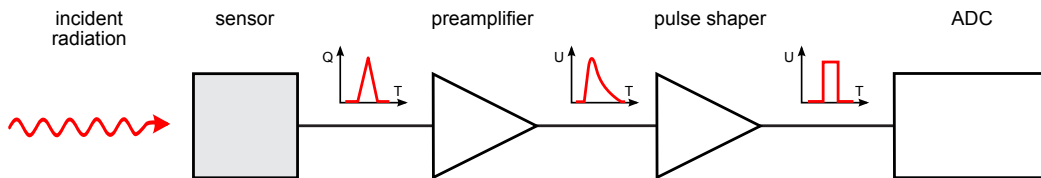
Figure 2.10: Schematic configuration of a basic semiconductor detector, adopted from Spieler [2006]. The curves marked red after the different detector components indicate the signal form at the corresponding stage.

Sensor Materials

An important part of the detector is its sensor. When it absorbs a photon, electron-hole pairs are generated since electrons are excited from the valence to the conduction band. An electric field established by the so called bias voltage U_{bias} separates the charges and directs them to the electrodes of the sensor. As the amount of charge, which arrives at the electrodes is proportional to the deposited energy, the energy of the absorbed photon can be determined.

One reason for a high U_{bias} is the time resolution, since the charge carriers should be swept quickly to the electrodes. The velocity v of the charges in a semiconductor is described classically in equation 2.4, whereas μ describes the mobility of the charge

carriers and E the strength of the applied electric field.

$$v(x) = \mu\, E(x) \tag{2.4}$$

Furthermore, the *charge collection efficiency* of the sensor is increased, because the chance of recombination of electron-hole pairs is reduced for a higher v. Other reasons for a high U_{bias} are a reduced *sensor polarisation* (see figure 2.13) and a reduced *inter pixel cross-talk* (IPCT), which is described in detail in section 2.2.3. Nevertheless, the limitation of U_{bias} is given by the fact that the signal current has to be higher than the current resulting from $I(\tilde{\rho}) = \frac{U_{bias}}{R(\tilde{\rho})}$, which depends on the maximum resistivity $\tilde{\rho}$ of the sensor material used. Additionally, a higher U_{bias} increases the effects of crystal defects, which are visible in the resulting images [Koenig et al., 2011 c].

In this part, silicon (Si) and cadmium telluride (CdTe) are discussed as semiconductor sensor materials as they are used most frequently. The parameters for both materials are listed in table 2.2.

		CdTe	Silicon
atomic number Z		48 / 52	14
density ρ	$\frac{\mathrm{g}}{\mathrm{cm^3}}$	5.85	2.33
electron mobility μ_e	$\frac{\mathrm{cm^2}}{\mathrm{Vs}}$	1100	1350
electron lifetime τ_e	s	$\sim 10^{-6}$	$\sim 10^{-3}$
$(\mu\tau)_e$-product	$\frac{\mathrm{cm^2}}{\mathrm{V}}$	$3 \cdot 10^{-3}$	>1
hole mobility μ_h	$\frac{\mathrm{cm^2}}{\mathrm{Vs}}$	100	450
hole lifetime τ_h	s	$\sim 10^{-6}$	$\sim 10^{-2}$
$(\mu\tau)_h$-product	$\frac{\mathrm{cm^2}}{\mathrm{V}}$	$2 \cdot 10^{-4}$	>1
dielectric constant ε		10.9	11.7
bandgap E_g[3]	eV	1.44	1.12
mean energy to produce an electron-hole-pair E_i	eV	4.43	3.6
intrinsic charge carrier density n	$\mathrm{cm^{-3}}$	$2 \cdot 10^6$	$\sim 10^{10}$
maximal resistivity $\tilde{\rho}$	$\mathrm{k\Omega\, cm}$	$5 \cdot 10^9$	40

Table 2.2: Parameters for two representative detector materials, adopted from Spieler [2006]; Greiffenberg [2010].

The production of large detector grade wafers is difficult, but is rewarded with good absorption in the energy range relevant to medical imaging. Other important advantages of the semiconductor CdTe are its wide band gap of $E_{g,CdTe} = 1.44\,\mathrm{eV}$ and its low intrinsic carrier density of $n_{CdTe} = 2 \cdot 10^6\,\mathrm{cm^{-3}}$, which lead to a high

---

[3]at room temperature

maximal resistivity of $\tilde{\rho}_{CdTe} = 5 \cdot 10^9 \, \text{k}\Omega \, \text{cm}$. The latter is high enough to use intrinsic CdTe as high resistivity, ohmic sensor material, in contrast to silicon, which is operated as a diode. $\tilde{\rho}_{Si} = 40 \, \text{k}\Omega \, \text{cm}$ is several orders of magnitude lower, which leads to a higher current flow than the signal current as well as heat. This problem can be solved by using a reversely biased pn-diode for applications with silicon. Then, a high electric field region depleted from free charge carriers with only a minor leakage current occurs. To minimise defects CdTe is often doped with chlorine (Cl) [Spieler, 2006].

Pulse Pile-Up

Pulse pile-up denotes the phenomenon of overlapping signals in the detector electronics, as illustrated in figure 2.11 b. In this case, the first signal has not decayed completely before another signal is detected. However, a further signal can only be detected after the previous signal has dropped below the discriminator level. To minimise this problem, either the shaping time T_{shape} for each pulse or the incident flux can be reduced. But then, other detector properties are typically influenced, too, as discussed in section 4.3.

(a) two detectable pulses   (b) pile-up   (c) shaped pulses
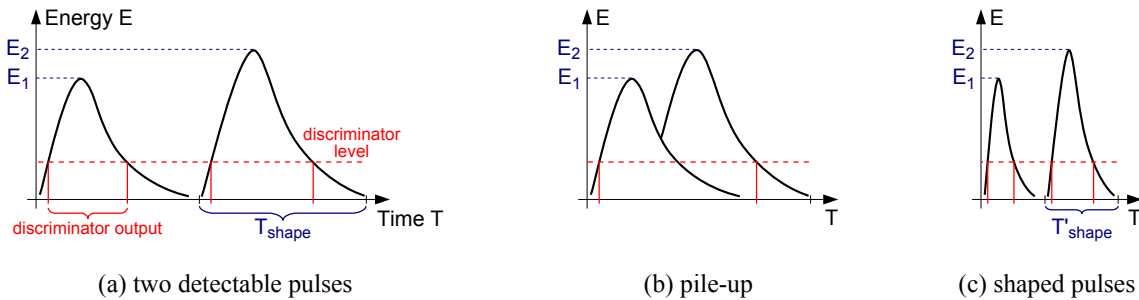
Figure 2.11: Illustration of the pile-up effect and pulse shaping. In (a), the time between the two pulses is long enough to detect both. In (b), the first pulse signal does not fall below the discriminator setting, which leads to pile-up. In (c), the shaping time is reduced and thus are both separable again.

There are two different types of pulse pile-up: Whereas in *paralysable pile-up* detectors an event during the signal time T_{signal} extends the dead time, in *non-paraysable pile-up* detectors an event during T_{signal} has no effect, as illustrated in figure 2.12 a. In this example the paralysable detector only detects three events, in contrast to the non-paralysable detector which detects four signals. A signal is counted when the pulse drops below the discriminator level.

However, pile-up can cause erroneous count-to-event rate measurements as in 2.12 b, but also erroneous energy measurements. While the photon rates can be corrected, the energy information is uncorrectable since the detected photons are counted as a single event with the sum of the energies.

(a) schematic detector answers

(b) analysed detector answers
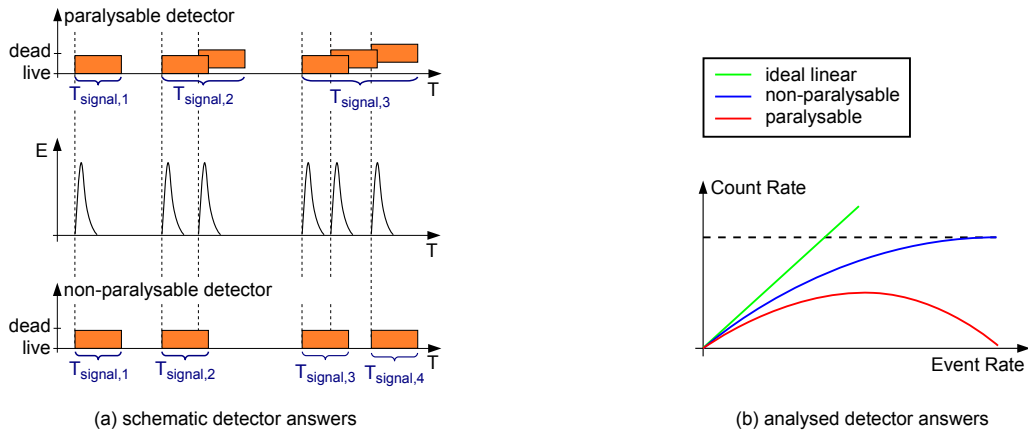
Figure 2.12: Differences between paralysable and non-paralysable detectors. In (a) a typical example is given. In (b) the pile-up effects of the count rates are shown. A non-paralysable detector always counts at least as much events as a paralysable detector. For spectroscopic applications, an ideal linear response is desired.

Sensor Polarisation

Sensor polarisation happens when trapped charges accumulate in the sensor and counteract the applied internal electric field generated by U_{bias}. As a consequence,

(a) an initial event

(b) initial polarisation

(c) progressed polarisation

(d) linearity deviation
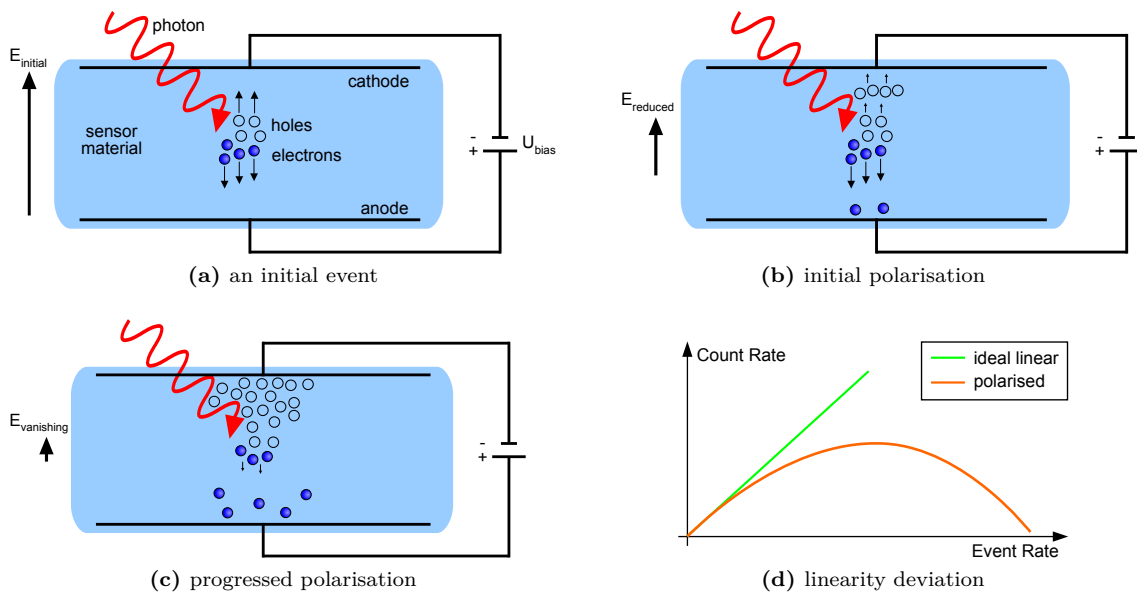
Figure 2.13: Sketches to illustrate polarisation in the sensor. After an initial event has occurred in (a), some charge carriers were trapped in (b), which makes it difficult for further charge carriers generated in subsequent events to reach the electrodes. In (c) the polarisation has progressed so far that it is nearly impossible for the charges to reach the electrodes. The effects of polarisation on the count rate are shown in (d) and resemble those of pulse pile-up (figure 2.12 b).

in the reduced electric field charges take longer to reach the electrodes and may be subject to increased trapping, which is shown in figure 2.13. Additionally, holes need more time than electrons to cross the same distance 2.2. The chart in figure 2.13 d clarifies the deviation of the desired linearity. But compared to figure 2.11 b, this deviation can happen at a completely different magnitude and various event rates (see also section 4.5) [Bale and Szeles, 2008].

2.2.3 Pixelated Detectors

In this section the setup and the read-out of Medipix2 pixel detectors are introduced. An overview of the Medipix detector family is given in subsection 2.2.4. The sensor material is connected to the readout electronics by intentionally ohmic contacts (section 2.2.1), which are made of small metal balls, called bump bonds. This is illustrated in figure 2.14. After photons with a higher energy than E_g generate electron hole pairs in the sensor, the charges are drawn to the readout electronics by U_{bias}, applied between the sensor material and the pixel cells.
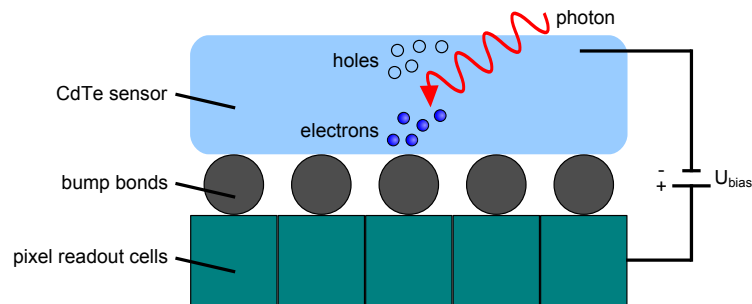
Figure 2.14: Schematic setup of the signal recording of the Medipix detector. A typical event is sketched in which electron-hole pairs are generated by an incoming photon.

The readout electronics of a Medipix2 application-specific integrated circuit (ASIC), which is illustrated in figure 2.15, offers both, a spatial and a spectral resolution. The former is obtained by the pixelated readout where the distance between bump bonds determines the spatial sampling rate. The spectral resolution can be realised since the amount of charge, which is detected by a pixel at a particular time, is proportional to the energy that the corresponding photon deposited in the detector. For spectral imaging the detector can be operated in two different modes: Either the detector is operated in *single threshold mode*, where only the lower energy threshold (THL) is set or in window mode, in which a low and high energy threshold (THL and THH) are adjusted. In this thesis, only the low threshold is used in order to avoid instabilities. The low threshold indicates the minimum energy which a photon must have to be counted in the Medipix array.

The electronics works as follows: At first, electric charges reach a charge sensitive preamplifier via the bump bonds. The output voltage of the preamplifier is proportional to the charges at its input. Afterwards, this voltage is compared to the
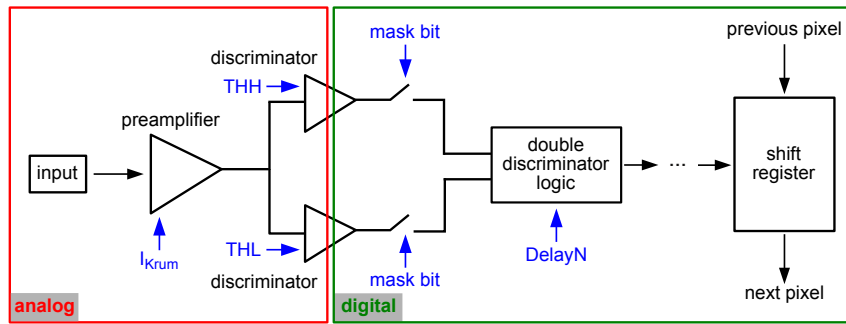
Figure 2.15: Sketch of a Medipix2 pixel cell, adopted from Llopart et al. [2002]. The input signal is compared to the threshold values. If the signal matches the given energy window the counter will be incremented by one.

low and / or high threshold voltages representing the THL and THH values in two different discriminators. Events are only counted in the following double discriminator logic when both discriminator requirements are fulfilled. In the next step, the data are written in a shift register with a maximum count rate per pixel of 1 MHz. The maximum counts per pixel in a measurement is limited to 11 810 due to the pseudo-random counter used [Llopart et al., 2002]. Finally, the ASIC is read out by the Pixelman software [Holy et al., 2006] via the FITPix USB interface [Kraus et al., 2011] and is transfered to an external computer. The Medipix2 MXR behaves as a paralysable detector (section 2.2.2).

The settings for the different digital-to-analog converters (DAC) can be changed in a control panel, which is shown in figure 2.16. The most used DACs in this master thesis are the DAC I_{Krum}, DelayN and THL. The constant current source I_{Krum} defines the discharge current of the preamplifier as well as the leakage current compensation of each pixel. For this purpose, an operational amplifier connected as an integrator is employed with further components, which is called Krummenacher circuit. This charge sensitive preamplifier is able to compensate a leakage current, which can arise in semiconductor detectors. The output signal features a steep increasing slope, which decreases slowly depending on the setting of the discharge current I_{Krum} [Krummenacher, 1991]. The digital signal at the output of the double discriminator logic can be adjusted by the DAC DelayN to a variable pulse width. The THL value determines the voltage setting of the low energy discriminator.

Inter-Pixel Cross-Talk (IPCT)

IPCT depends on the pixel pitch of the detector and is therefore a determining factor for the image quality. To obtain a high spatial resolution, a small pixel pitch is desired. Nevertheless, a large pixel pitch provides a high spectral resolution. The latter is mainly due to *charge sharing* and *characteristic X-rays*.
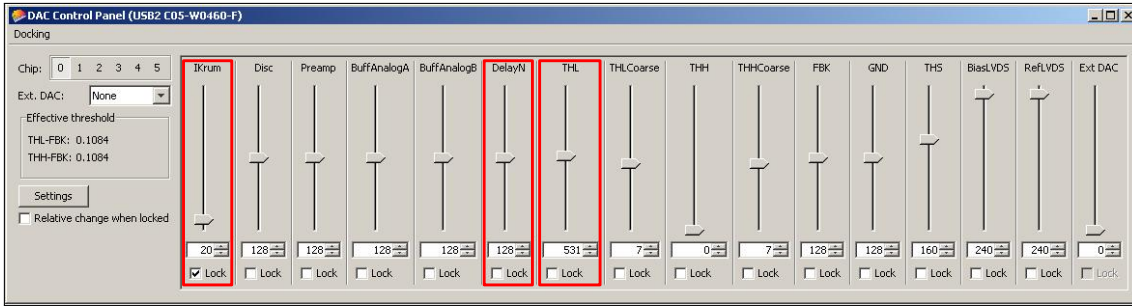
Figure 2.16: The DAC control panel from the Pixelman software. The most important DACs for this thesis are the I_{Krum}, DelayN and THL, marked with red boxes.

Charge sharing occurs when charges generated in the sensor by a photon interaction are spread over several pixels. This effect is caused by diffusion and leads to events, in which a photon with high energy is detected as multiple photons with lower energies, as can be seen in figure 2.17 a. This problem can be minimised by connecting just every n^{th} pixel to a bump bond. A larger pixel pitch is provided when the remaining pixels are connected to their neighbours. This technique is called *binning* and is illustrated for every second pixel in figure 2.17 b.

Charge sharing depends on the incoming photon energy and increases at higher photon energies. This is due to a higher number of charge carriers, which will spread more. Furthermore, charge sharing is less pronounced for higher bias voltages since then the charge carriers move faster to the bump bonds and hence suffer less from diffusion [Koenig et al., 2012].

(a) charge sharing

(b) 2×2 binning
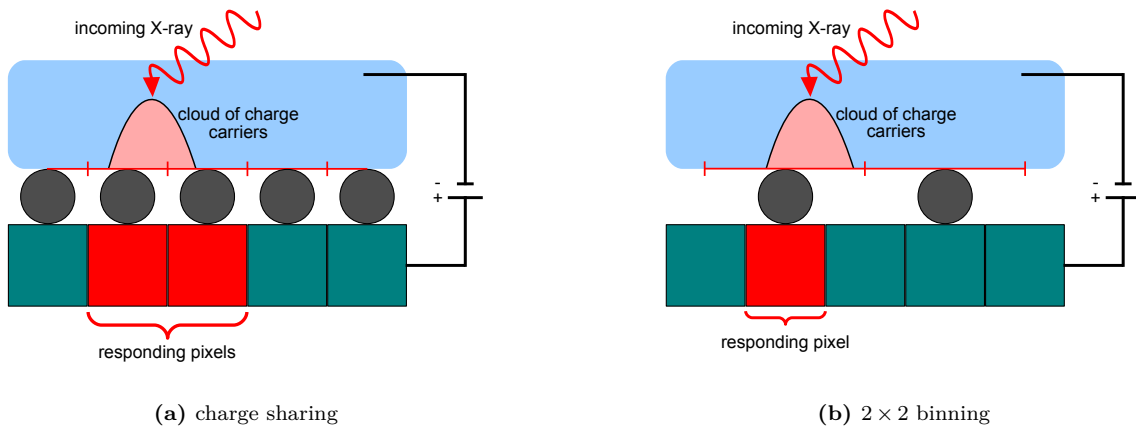
Figure 2.17: IPCT in terms of charge sharing, shown for different pixel pitches. The pixels marked red correspond to the responding pixels for the sketched events.

Characteristic X-rays describe the effect of unintended *fluorescence peaks* and their *escape peaks* at the pixel's energy response, which do not correspond to the incoming radiation. These peaks have their origin in the sensor material and occur when an incoming photon has enough energy to knock an electron out of its atomic

shell. The fluorescence photon is generated when the gap is again closed by an electron and the energy difference between the two shells corresponds to the energy of the emitted photon. At the applied detectors only the transition $K_{\alpha 1}$ is considered since it is the most probable spectral line. For CdTe the energies of the fluorescence photons are $E_{fl,Cd} = 23.2\,keV$ and $E_{fl,Te} = 27.5\,keV$. If the incident photons are monochromatic with the energy E_0 the escape peaks will be characteristic as well, since $E_{escape} = E_0 - E_{fl}$. For a broadband X-ray spectrum the escape peaks form a continuous background at low energies. A fluorescence and escape peak will be measured in the energy response function if the fluorescence photon is able to reach a neighbouring pixel. Then, E_{escape} is detected at the original and E_{fl} at the neighbouring pixel. This depends on the mean free path lengths, which are $\bar{l}_{fl,Cd} = 119\,\mu m$ and $\bar{l}_{fl,Te} = 62\,\mu m$ in CdTe and in the order of the detector's pixel pitches [Tlustos, 2005; Shikhaliev et al., 2009].

2.2.4 The Medipix Detector Family

Hybrid pixel detectors for tracking applications in high energy physics were developed for the large hadron collider (LHC) at the European Organisation for Nuclear Research (CERN) in Geneva. To distribute this technology to other fields of science, the Medipix Colaboration[4] was founded.

Medipix1

With the Medipix1 assembly it is possible to realise single photon counting X-ray imaging. This technique enables to take images that do not exhibit a dark current, which is called noise-free imaging. The direct X-ray conversion in a semiconductor sensor minimises image blurring and avoids an extra conversion stage from X-rays into visible light (see section 2.1.3). The Medipix1 is a complementary metal oxide semiconductor (CMOS) imaging chip and features square pixels of 170 µm side-length, combined to 64×64 pixels per chip. Silicon and gallium arsenide (GaAs) sensors can be bump-bonded due to a read-out of positive charges. The electronics of the Medipix detectors is explained in more detail for the Medipix2 MXR, which is used in this thesis, in section 3.1.3. In the Medipix1 detector incoming charge is processed and then compared in a comparator circuit with a given threshold. If the signal exceeds this threshold, which corresponds to a certain energy, the event will be counted. For that reason, noise performance of the detector follows the theoretical limits of Poissonian statistics which results in a high SNR [Campbell et al., 1998].

Medipix2 & Timepix

For the Medipix2 detector the pixel size is reduced to 55 µm side-length for a square pixel. Furthermore, the number of pixels per chip is increased to a total of 256×256 pixels. The construction of the chip is enhanced compared to the Medipix1 so that both positive or negative input charges are accepted. This leads to alternatives in

---

[4]Medipix homepage [Online; accessed 20-October-2012]:
http://medipix.web.cern.ch/medipix

the choice of the sensor material, such as CdTe. Additionally, with the Medipix2 assembly it is possible to select not only a lower energy threshold but also an energy window [Llopart et al., 2002].
The Medipix2 MXR is a redesign of the Medipix2 chip and features an improved radiation hardness as well as an increased counter depth, which has been increased from 8 192 (13 bits) to 11 810 due to a pseudo-random counter used.

A further development resulted in the Timepix chip. Although it only features a single energy threshold, it offers three different modes, named single particle counting (Medipix mode), arrival time (Timepix mode) and time over threshold (ToT). In Medipix mode, the readout counts single photons using a low energy threshold only. In the case of the other modes a clock pulse coupled to each pixel is employed. By doing so it is possible to determine the arrival time of a photon compared to the shutter signal. The shutter defines the final point of a measurement. Furthermore, in ToT it is possible to measure the time in which the electrical signal of the generated pulse exceeds the given threshold. This quantity is correlated with the deposited energy of a detected photon and thus offers true spectroscopic performance. However, this mode does not allow multiple hits per pixel, which makes it unsuitable for imaging applications [Llopart et al., 2007].

Medipix3

The Medipix3 readout architecture can be operated in single pixel mode, in charge summing mode or in spectroscopic mode. In summing mode, the assembly is able to reduce the effects of charge sharing by comparing the signals of neighbouring pixels. This is done by summing up charges generated simultaneously in neighbouring pixels and assigning the sum to the individual pixel with the highest collected charge. In spectroscopic mode, it is possible to bump-bond only one out of four pixels, whereas the sensor's pixel pitch is increased from 55 μm to 110 μm. Each pixel has two thresholds and two counters, which enable the detector to read and write simultaneously. Hence, so called colour imaging and dead time free operation is possible by making use of the counters in the unconnected pixels [Ballabriga et al., 2007].

3 Materials & Methods

This chapter starts with illustrating the experimental setup describing the X-ray tube employed, the phantom layout and the photon counting detectors employed. Afterwards, calibration and imaging techniques used for the Medipix images are explained. Another section details the CT reconstruction methods used in this work.

3.1 Experimental Setup

The experimental setup[5] is placed in a shielded room to protect the experimenter as well as the surroundings and is illustrated in figure 3.1.

1) X-ray tube
2) rotary stage
3) holder for the phantom
4) holder for the source
5) Medipix detector
6) water cooling
7) adjustment motors
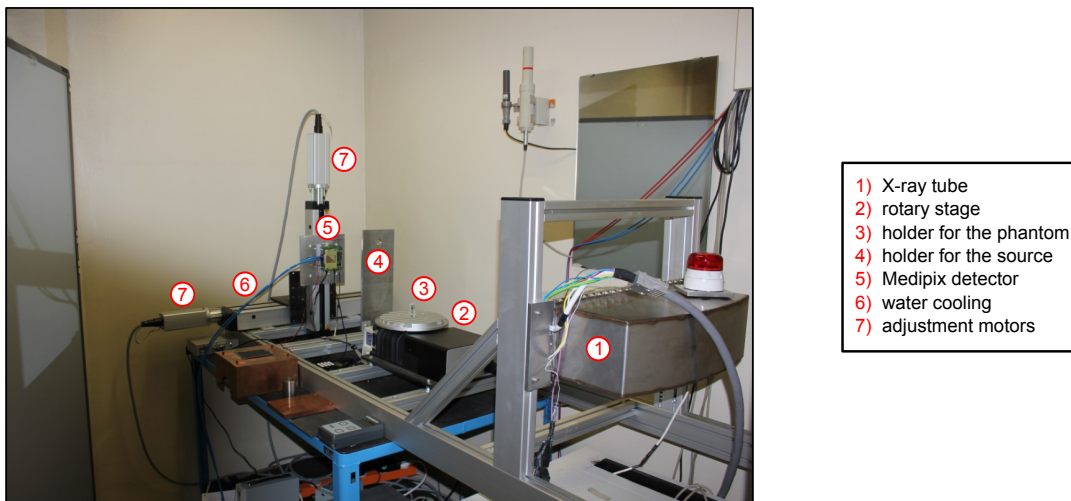
Figure 3.1: The experimental setup placed in a shielded room. The X-ray tube is shown on the right, the phantom is placed on the rotary stage in the centre and the Medipix detector can be seen in the background. For calibration an ^{241}Am source is used, which is placed directly in front of the detector.

The X-ray tube emits a continuous X-ray spectrum whose characteristics depend on the tube settings. The radiation is partly absorbed by the phantom fixed on a rotary table, that is necessary for CT imaging, at a distance of 54 cm from the X-ray tube. Afterwards, the radiation is analysed by a Medipix2 MXR detector at a fixed distance of 139 cm to the X-ray tube. This distance could be measured with a deviation of 1 cm by the aid of a mega-voltage (MV) CT, whereby the focal point

---

[5]constructed by Dr. Thomas König (DKFZ)

of the X-ray tube was determined (figure 4.3). The detector can be moved in the projection plane by means of two stepper motors. Since the X-ray tube emits a cone beam (section 3.3), the phantom appears larger on the detector the nearer it is placed to the tube. An advantage of the geometry chosen is the reduction of scatter in the imaging plane due to the large object-to-detector distance. The settings for the measurements as well as the selection of the motor are controlled by a computer outside the shielded room. For the CT measurements the rotary table is controlled by a software plug-in[6] to Pixelman.

For energy calibration purposes (section 3.2.2) a radioactive americium (^{241}Am) source can be placed directly in front of the detector [Schulze, 2011].

3.1.1 X-Ray Tube

For the CT and count rate measurements, a Siemens Powerphos X-ray tube is employed (figure 3.2), featuring a maximum tube current of 250 mA. By design, it can be operated in fluoroscopic mode below currents of 10 mA and in pulse mode above 10 mA. The tube voltage can be varied between 40 and 125 kVp, corresponding to mean photon energies of 31 and 60 keV[7]. These energies were simulated by Monte Carlo simulations, which are explained in detail in section 4.1. The size of aperture can be changed mechanically but was completely open for most of the measurements. The tube is cooled by a customary fan when running.
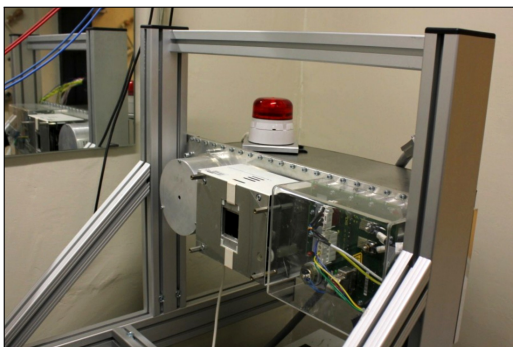
Figure 3.2: Photograph of the X-ray tube used throughout this work.
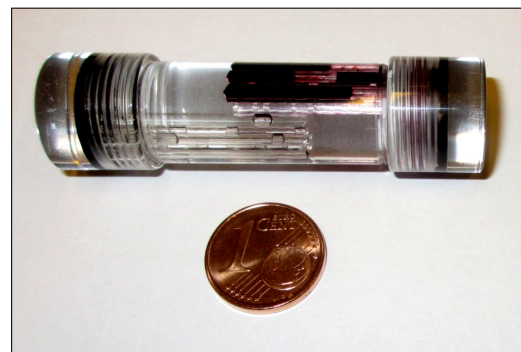
Figure 3.3: Photograph of the CT phantom.

3.1.2 Phantom Layout

A phantom[8] filled with contrast agents is used in order to imitate blood vessels. The phantom is made of polymethyl methacrylate (PMMA) and is illustrated in figures 3.3 and 3.4. It contains capillaries with diameters of 0.8 mm and 1.6 mm, which were

---

[6]written by Dr. Thomas König (DKFZ)

[7]Siemens AG, X-ray tube simulations [Online; accessed 20-October-2012]: `https://w9.siemens.com/cms/oemproducts/Home/X-rayToolbox/spektrum/Pages/radIn.aspx`

[8]designed and constructed by Julia Schulze, Armin Runz and Dr. Thomas König (all DKFZ)

filled with Imeron 300 (iodine) and Multihance $0.5\,\mathrm{M}$ (gadolinium) in this thesis. These represent common contrast agents in CT and MRI. Both contrast agents are present in five different concentrations c, as given in table 3.1 [Schulze, 2011].

(a) frontal point of view   (b) transversal point of view
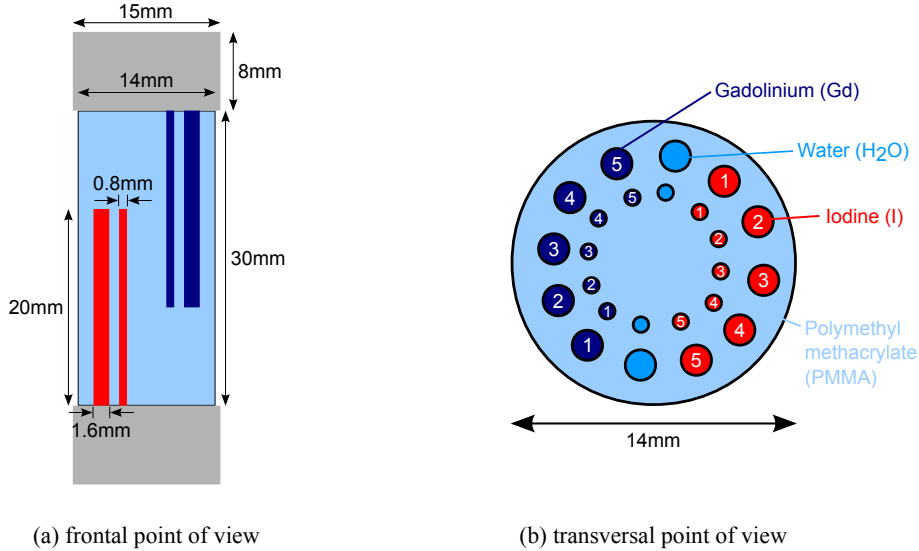
Figure 3.4: Sketches of the X-ray phantom [Schulze, 2011]. The red and blue marked capillaries are filled with contrast agents of different concentrations (compare the numbering with table 3.1).

capillary	$\mathrm{mc}_I\ \left[\frac{mg}{ml}\right]$	$\mathrm{mc}_{Gd}\ \left[\frac{mg}{ml}\right]$	$c\ \left[\frac{\mu mol}{ml}\right]$
1	31.8	39.4	250
2	6.36	7.88	50
3	3.18	3.94	25
4	1.90	2.36	15
5	1.27	1.58	10

Table 3.1: Contrast agent concentrations present in the phantom capillaries, adopted from Schulze [2011]. The equivalent mass concentrations mc were calculated by c times the molar mass M ($M_I = 127\,\frac{g}{mol}$ and $M_{Gd} = 158\,\frac{g}{mol}$).

3.1.3 Detectors

In this work, detectors of the generation Medipix2 MXR were used for the experiments. This type of detector device is attached to a semiconductor sensor via bump bonds. The two detectors studied consist of 3×2 Medipix2 MXR chips with a pixel pitch of $165\,\mu\mathrm{m}$ (Hexa, $4.2 \times 2.8\,\mathrm{cm}^2$) and 2×2 chips with a pixel pitch of $110\,\mu\mathrm{m}$ (Quad, $2.8 \times 2.8\,\mathrm{cm}^2$), as illustrated in figure 3.5 [Koenig et al., 2012]. Both feature

a 1 mm thick CdTe sensor, made of a single crystal. Due to its thickness the detection of high energy photons is enabled, as they mostly lose their whole energy when passing through the sensor.

The CdTe crystals[9] are grown by the *travelling heater method*, which accomplishs a high homogeneity of the crystal [Funaki et al., 1999]. However, since CdTe is not understood as well as silicon, sensor qualities do not reach optimal quality, yet. This results in insensitive areas in the X-ray images caused by increased leakage current [Koenig et al., 2011 c].
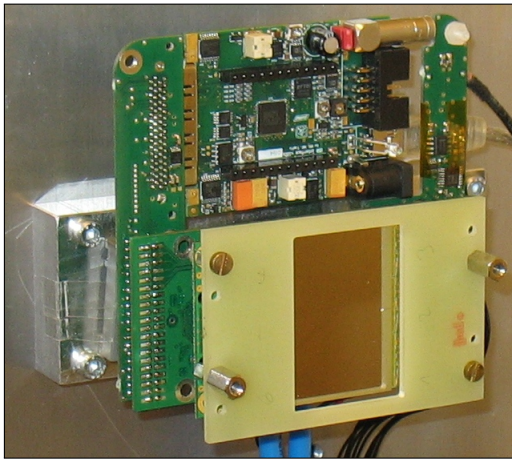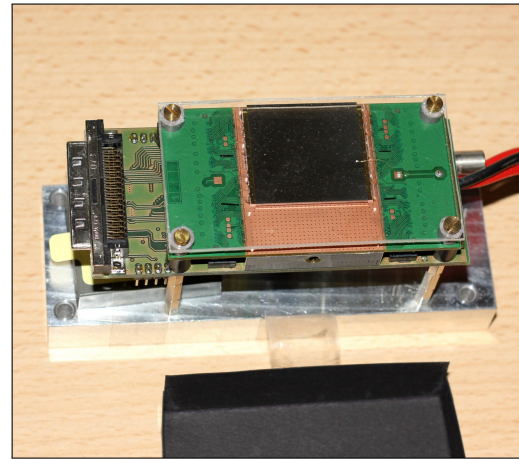
(a) Medipix2 MXR hexa detector   (b) Medipix2 MXR quad detector

Figure 3.5: Photographs of the two MXR multi-chip assemblies used in this work. The reflecting surfaces in the centre of the devices represent the sensors, which are covered by silver (Ag) electrode coatings.

In this work, the bias voltage at the sensor is set to - 400 V for nearly all measurements in order to reach a high spectral resolution but small leakage current dependent image artefacts [Koenig et al., 2011 c]. The negative sign of U_{bias} indicates, that with the intrinsic CdTe detectors electrons are counted in the following readout electronics instead of holes, as in silicon detectors (section 2.2.2).

The detectors are operated at room temperature and therefore a water cooling is installed to protect the sensor from detaching due to different thermal expansion coefficients of silicon and CdTe. Furthermore, thermally excited electron hole pairs created in the sensor material are avoided. In order to prevent radiation damages the detector is protected by a coverage made of copper (Cu) during the measurements, not visible in figure 3.5.

---

[9]fabricated by the Japanese company Acrorad

3.2 Calibration & Imaging Techniques

Prior to the measurements, a threshold equalisation and an energy calibration have to be performed. Both methods are described in detail below. Furthermore, some simple digital image processing steps are explained. The evaluation for the measured equalisation data and further image processing steps have already been implemented[10] in the programming languages R[11] and C++ and are used for this thesis.

3.2.1 Threshold Equalisation

A threshold equalisation is necessary since every pixel behaves individually and the thresholds for energy discrimination can only be set for whole chips. Hence, each pixel offers three switchable current sources controlled by three bits, whose optimal settings have to be determined prior to the measurements. The aim of the threshold equalisation is to minimise the actual threshold positions between the pixels in one chip. In this thesis, two different types of equalisation methods, named *image homogeneity calibration* and *peak position calibration*, were used and are explained in detail below [Koenig et al., 2011 b; Zuber, 2010].

Spectral Equalisation

The spectral equalisation is a characteristic calibration technique, which is stable for energy drifts. Hence, it is useful for measurements at different mean energies, set in a polychromatic spectrum by the X-ray tube.
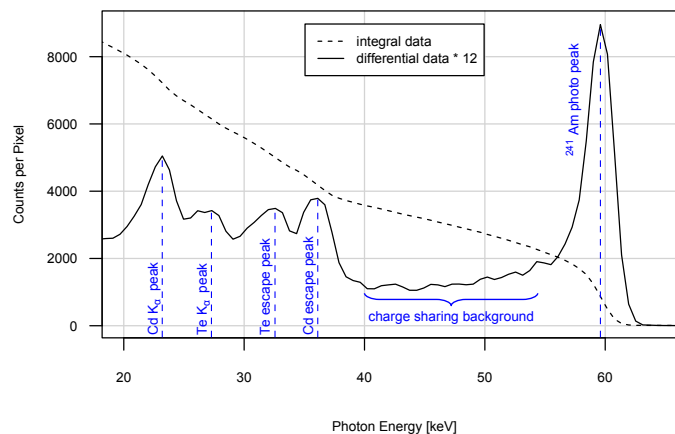
Figure 3.6: Integrated and differentiated energy calibration curves for chip 4 of the hexa detector. The blue inserts indicate the most important energy peaks.

---

[10]written by Marcus Zuber (DKFZ)
[11]http://www.r-project.org/

First, two THL DAC scans with the THL adjustment bits set to 0 and 7 have to be performed by using the ^{241}Am source. A plug-in for the Pixelman software is used to scan the THL DAC range automatically. Therefore, the plug-in starts with a given higher value than the expected ^{241}Am photo peak and lowers the THL setting in specific steps. The counts increase in this reverse scanning process, which is started at high threshold values, and can be displayed as integrated data similar to figure 3.6.

After scanning the data are differentiated and so the ^{241}Am photo peak positions for each pixel are determined. Finally, a configuration for the three bits is determined for each pixel such that the resulting peak positions are as close as possible across a chip. Thereby, linearity of the peak positions is assumed when the adjustment values are altered. The histogram of a typical equalisation can be seen in figure 3.7.
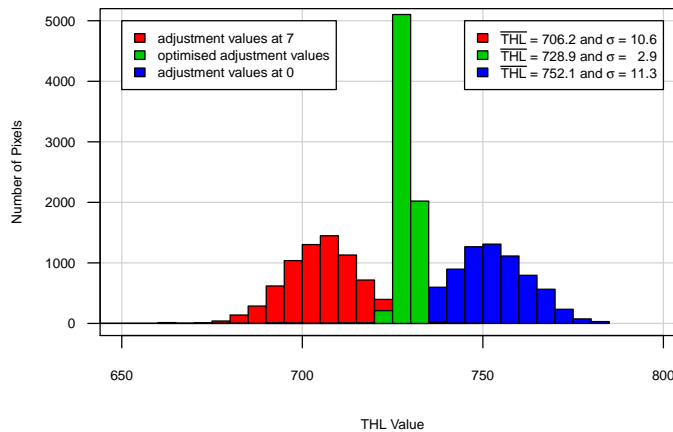
Figure 3.7: Number of pixels with a given photopeak location for chip 4 of the hexa detector. The high and narrow green bars indicate a successful threshold equalisation.

Table 3.2 illustrates the results of a typical threshold equalisation, where σ represents the standard deviation for the photopeak position. Chip 4 is highlighted because it has the lowest σ for the optimised bits. This is the reason why most of the measurements only consider the analysis of this chip.

Image Homogeneity Equalisation

The advantage of the homogeneity equalisation method compared to the spectral equalisation is the achievement of an equal intensity response of each pixel. It can be performed easier and faster, but does not guaranty a good spectral resolution between the pixels. At the beginning, a specific energy has to be set employing the X-ray tube. The following measurements have to be carried out with this energy as

	Adjustment Values $= 7$		Optimised Bits		Adjustment Values $= 0$	
	$\overline{THL}_7$	σ_7	$\overline{THL}_{opt}$	σ_{opt}	$\overline{THL}_0$	σ_0
Chip 0	715.8	11.6	739.1	9.0	760.7	11.8
Chip 1	697.3	13.0	712.9	23.3	740.9	15.9
Chip 2	707.5	11.1	730.2	8.1	751.5	11.8
Chip 3	694.4	11.1	713.9	11.8	737.1	12.0
Chip 4	706.2	10.6	728.9	2.9	752.1	11.3
Chip 5	700.1	10.8	722.3	6.8	745.7	11.8

Table 3.2: Results of a typical threshold equalisation, as shown in the histograms in figure 3.7. For chips 1 and 3 σ_{opt} is higher than for the other chips since there are more pixel defects.

well. Afterwards, flatfield images, which are radiographs without any object, with the THL adjustment bits set to 0 and 7 have to be recorded. To minimise the SNR a couple of images should be acquired. Then, for each chip the optimised THL value (THL_{opt}) is calculated:

$$THL_{opt} = \frac{\overline{THL}_{adj.\,values=7} + \overline{THL}_{adj.\,values=0}}{2} \tag{3.1}$$

Finally, each adjustment value of every pixel is set as close as possible to THL_{opt}, assuming that the intensity depends linearly on the adjustment values.
After the threshold equalisation process, the adjusted bit values are saved in a pixel mask, which has to be loaded before the upcoming measurements. A typical THL mask is shown in figure 3.8. In the centre of the whole sensor, more pixels are set to a higher bit value than in the periphery. This phenomenon is not completely understood, but a probable reason could be readout failures.
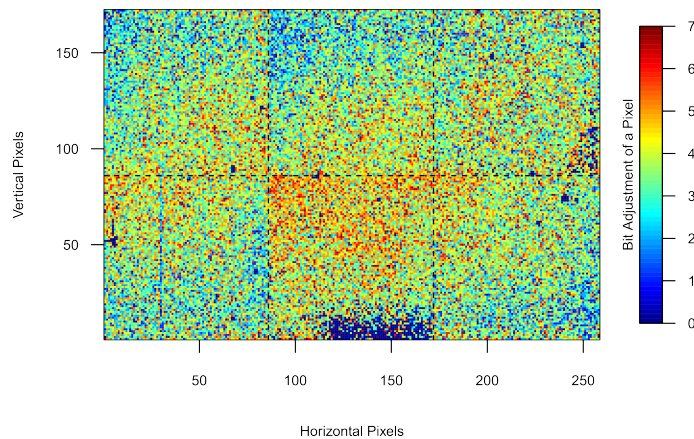
Figure 3.8: Typical pixel mask, which is produced in the threshold equalisation process. In the centre of the mask, more pixels are set to higher adjustment values than in the periphery.

3.2.2 Energy Calibration

The energy calibration is necessary to assign specific energies to the THL DAC values. For this reason, three different well visible peaks of the chip answer are used: These are the ^{241}Am photo peak at 59.6 keV, the Cd K$_{\alpha 1}$ peak at 23.2 keV and its associated escape peak at 36.4 keV. The peaks are obtained by irradiating the detector with the monoenergetic americium source and are shown in figure 3.6. The integral data have to be differentiated to visualise the different peaks and the background [Koenig et al., 2011 c].

The Medipix2 MXR detectors have an equivalent noise charge (ENC) of approximately 110 electrons. This is the number of electrons, which have to be collected in order to measure a signal equivalent to the noise of the detector. The ENC describes the error, which is gained by the preamplifier and discriminator while processing the signals. Hence, for the energy calibration an error of 3.5 threshold values succeeds [Spieler, 2006].

3.2.3 Digital Image Processing

To improve the quality of images several digital image processing steps are used as demonstrated in figure 3.10. The projections originate from an in-ear headphone, illustrated in figure 3.9. The headphone is used as a sample since it contains several small components with different absorption coefficients.

Figure 3.9: Photograph of the measured headphone.

The first step used to improve the original image (a) is a *flatfield weighted correction* shown in (b), which filters overexposed pixels and corrects steady inhomogeneities. This is done by mathematically dividing the measured pixel counts of (a) by a flatfield image, which has to be obtained at the same settings.

In example (c), a *defect correction* combined with a *median filter* is applied to (b). A median filter sets every pixel to the median value of its four next neighbours and its initial value. This is is done in two iterations in this case. But to avoid undefined
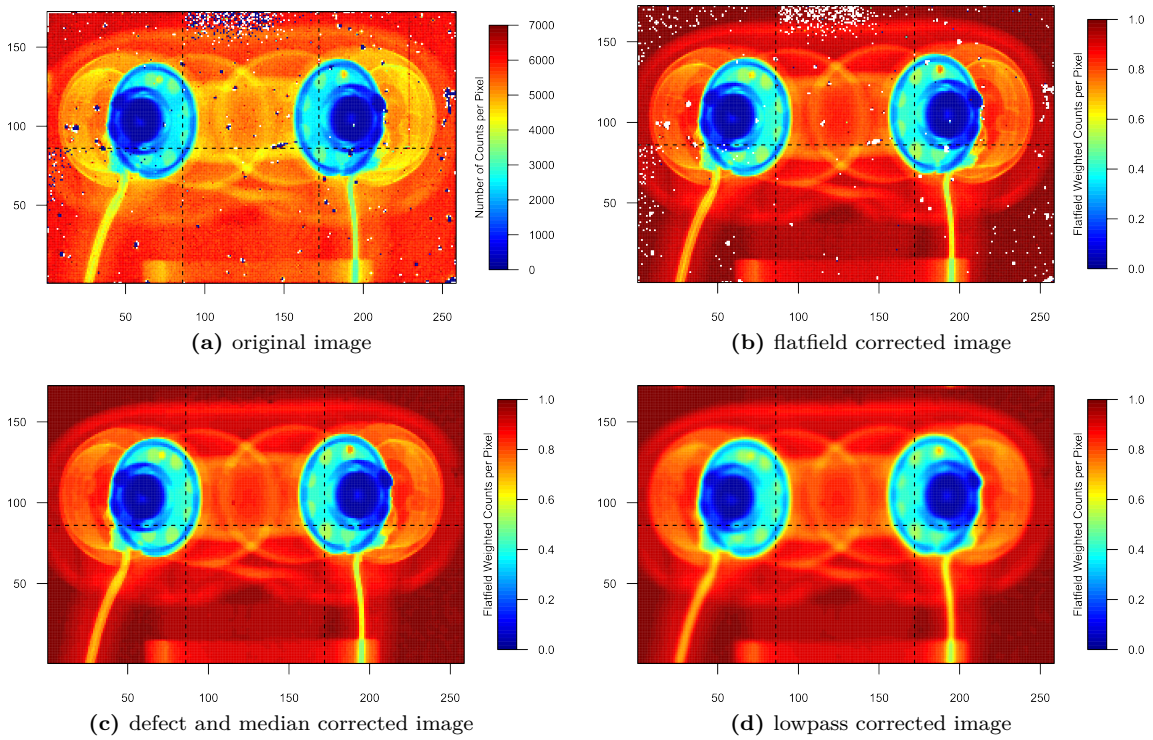
Figure 3.10: Projections of the headphone. Shown are the results of various image processing steps.

spots, pixels which do not have a finite value have to be resolved beforehand. This is done by defect correction, which works like a median filter for infinite pixel values, whereas surrounding infite pixel values are neglected. A median filter is a nonlinear filtering technique that removes noise but conserves edges in an image. The median is the numerical value, which separates the higher half of a sorted distribution from the lower half.

The *lowpass filter* used in (d) works like a binomial filter, which weights the pixels at the boundaries by the binomial coefficients. This technique leads to a smoothing of the image. The binomial coefficient with $n \in \mathbb{N}$ is defined as $\binom{n}{k} = \frac{n!}{k! \cdot (n-k)!}$, whereas n represents the filter area. In this example $n = 2$, which leads to a smoothing by the four next neighbouring pixels.

3.3 CT Reconstruction

This section describes the CT reconstruction algorithm used in this thesis. Absorption effects of X-rays with matter have already been discussed in section 2.1.2 and are the basis of CT images. For describing the reconstruction algorithm, equation 2.1 has to be extended for inhomogeneous objects and for polychromatic incoming

radiation:

$$\implies N = \int\limits_{0}^{E_{max}} N_0(E) \cdot e^{-\int_0^{\Delta x} \mu(s,E)\,ds}\,dE. \tag{3.2}$$

The absorption of incoming radiation by an inhomogeneous object is illustrated in figure 3.11. The aim of the reconstruction is to determine the spatial distribution of the absorption coefficients $\mu(x,y,z)$, respectively $\mu(x,z)$ for one slice of the CT reconstruction. Therefor N_0 can be obtained by a flatfield image and N results from several projections of different directions.

(a) homogeneous object   **(b)** inhomogeneous object
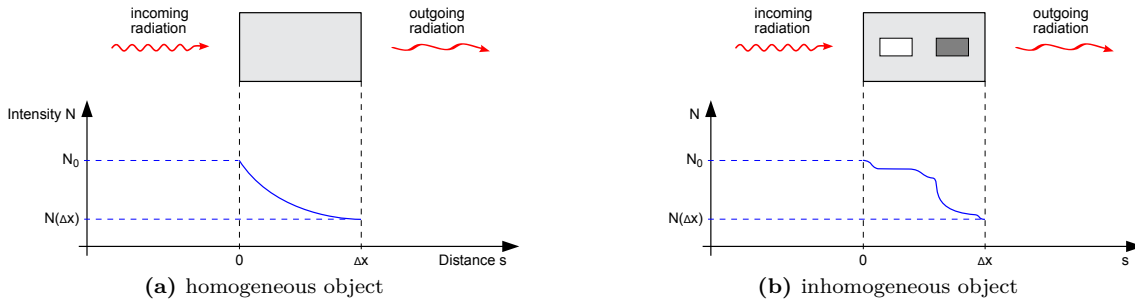
Figure 3.11: Absorption of radiation at different kind of objects. In both cases the resulting intensity is the same although the object is different. To analyse the inner parts of the objects a CT image can be made, whereby the object is irradiated from several angles.

The projection data P is transformed according to equation 3.3. Note that P is independent of the intensity of the incident X-ray beam except noise.

$$\implies P := -ln\left(\frac{N}{N_0}\right) = \int\limits_{path} \mu(\vec{x}) \cdot ds \tag{3.3}$$

Different CT reconstructions have to be considered depending on the radiation patterns. Most important are the two dimensional (2D) parallel and fan beam geometries as well as the three dimensional (3D) cone beam geometry, which are illustrated in figure 3.12.

The experimental setup features a cone beam geometry, because a larger area can be irradiated than in a parallel beam geometry. But it should be noticed that for a reconstruction of a centred single row, as applied, a cone beam reduces to a fan beam geometry, provided that scatter can be ignored. The following subsection describes the parallel beam reconstruction for a better understanding of this thesis.

(a) parallel beam   (b) fan beam   (c) cone beam
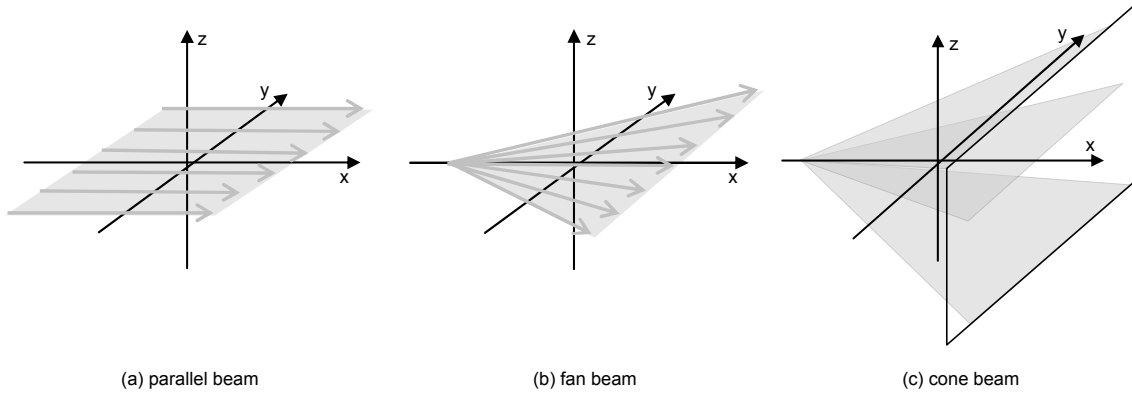
Figure 3.12: Different radiation patterns for CT, adopted from Quan [2009]. While (a) and (b) indicate 2D patterns, the pattern in (c) proceeds similar to (b) but in three dimensions.

As the CT reconstruction for the applied setup has already been realised[12], a detailed explanation of the fan beam reconstruction can be found in Schulze [2011]. This is done by selecting a set of parallel beams from fan beams at various angles.

3.3.1 Parallel Beam Reconstruction

For the parallel beam reconstruction equation 3.3 can be rewritten as a line integral in the 2D plane. The result is shown in equation 3.4, which is named 2D *Radon Transform* of the function $\mu(\vec{x})$. Therefor, a unit vector $\vec{n}$ is used, that is in the xy-plane and orthogonal to the beam direction. Furthermore, a path through the object is parametrised with ϑ and r. The Radon Transform in equation 3.4 relates to the 2D distribution of linear attenuation coefficients to its projection data, so that the inversion of the Radon transform produces the reconstruction of the 2D function. The projection geometry is indicated in figure 3.13.

$$\implies P(\vartheta,r) = \int\limits_{-\infty}^{\infty} \int\limits_{-\infty}^{\infty} \mu(\vec{x}) \cdot \delta(x\,cos(\vartheta) + y\,sin(\vartheta) - r)\,dxdy \tag{3.4}$$

$$\text{with} \quad \vec{n} = [cos(\vartheta), sin(\vartheta)]^T$$
$$\vec{x} \cdot \vec{n} - r = x\,cos(\vartheta) + y\,sin(\vartheta) - r = 0$$

The *Fourier Slice Theorem* says that the one dimensional (1D) Fourier transform $\mathcal{F}^1$ of a projection of an object is equal to one slice of the 2D Fourier transform $\mathcal{F}^2$

---

[12]implemented by Dr. Thomas König and Julia Schulze (both DKFZ)

(a) parallel projections   **(b)** parallel geometry
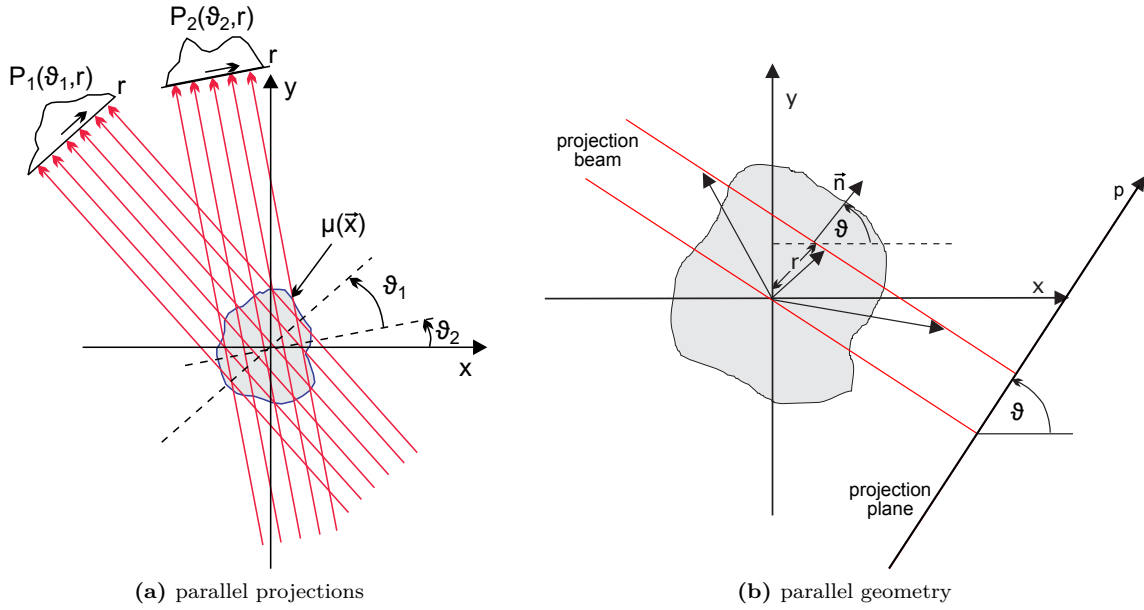
Figure 3.13: Projections and geometry for parallel beams in CT, adopted from Jähne [2005]. The red marked arrows in (a) indicate the radiation, which is absorbed by the object $\mu(\vec{x})$ from different angles ϑ_i to obtain a CT image. This leads to different projections P_i of the object. In (b), the red marked lines indicate a single projection beam.

of the object, as can be seen in equation 3.5.

$$\mu(x,y) = \mathcal{F}^{-2}\left\{\sum_{projections} \mathcal{F}^1[P(\vartheta,r)]\right\} \tag{3.5}$$

To demonstrate the Fourier Slice Theorem, which is illustrated in figure 3.14, a simple case with $\vartheta = 0$ is considered. Then $r = x$ and it follows equation 3.6:

$$P(0,x) = \int_{-\infty}^{\infty} \mu(x,y) \cdot dy \tag{3.6}$$

$$\Longrightarrow \mathcal{F}^1[P(\vartheta,r)] =: \mathcal{P}^1(0,k_x) = \int_{-\infty}^{\infty} P(0,x) \cdot e^{-ik_x x}\, dx$$

$$= \int_{-\infty}^{\infty}\left[\int_{-\infty}^{\infty} \mu(x,y) \cdot dy\right] e^{-ik_x x}\, dx$$

$$\Longrightarrow \mathcal{F}^2[\mu_{k_y=0}(x,y)] = \int\limits_{-\infty}^{\infty} \int\limits_{-\infty}^{\infty} \mu(x,y) \cdot e^{-ik_x x} \underbrace{e^{-i \cdot 0 \cdot y}}_{=1} dxdy$$

$$=: \hat{\mu}^2(k_x, k_y = 0) \overset{!}{=} \mathcal{P}^1(k_x, k_y = 0).$$
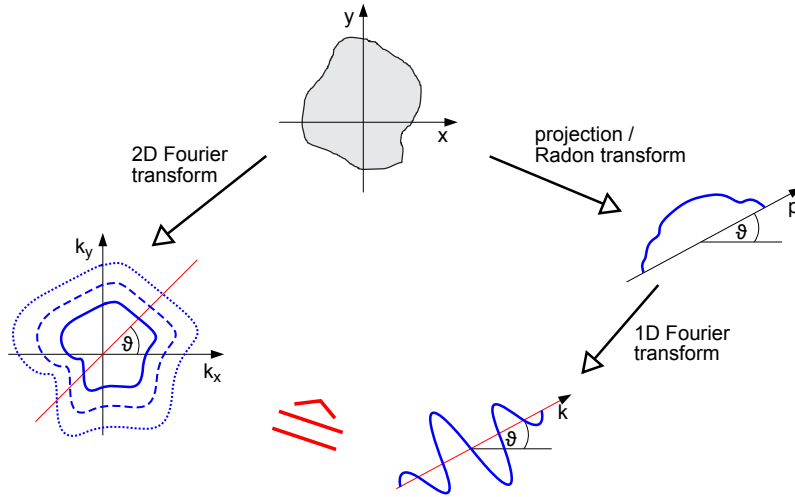
Figure 3.14: Schematic illustration of the Fourier Slice Theorem: A 1D Fourier transform of a projection of the object is equal to one slice of the 2D Fourier transform of the object [Schlegel and Bille, 2002].

3.3.2 Practical Implementation

Although the whole principle of CT is based on the Fourier Slice Theorem, in practice CT reconstruction is performed differently. Instead, polar coordinates in the frequency domain are used in order to emphasise edges in the image and to avoid a higher sampling rate for the centre of the projected object than for the outer parts. Otherwise, complicated interpolation strategies in the Fourier domain would be required. This leads to:

$$\Longrightarrow \mu(x,y) = \int\limits_{-\infty}^{\infty} \int\limits_{-\infty}^{\infty} \hat{\mu}^2(k_x, k_y) \cdot e^{i(k_x x + k_y y)} dk_x dk_y$$

$$= \int\limits_{0}^{2\pi} \int\limits_{0}^{\infty} \hat{\mu}^2(\vartheta, |k|) \cdot e^{i|k|(x\cos(\vartheta) + y\sin(\vartheta))} |k| \, dk d\vartheta. \tag{3.7}$$

This equation can be simplified and the 2D Fourier transform $\hat{\mu}^2(\vartheta, |k|)$ can be

replaced by the 1D Fourier transform $\mathcal{P}^1(\vartheta, |k|)$ of the projection:

$$\Longrightarrow \mu(x,y) = \int\limits_{0}^{\pi} \underbrace{\int\limits_{-\infty}^{\infty} \mathcal{P}^1(\vartheta, |k|) \cdot |k| \; e^{i|k|r} \, dk}_{=:Q(\vartheta, r)} \, d\vartheta \tag{3.8}$$

with $\quad \hat{\mu}^2(\vartheta + \pi, |k|) = \hat{\mu}^2(\vartheta, -|k|)$
$\quad\quad\quad r = x \cos(\vartheta) + y \sin(\vartheta).$

Thus, to obtain a reconstructed image mainly two steps have to be accomplished: First, a filtering needs to be performed, for which a 1D Fourier transform of the projections is combined to obtain $\mathcal{P}^1$. After $\mathcal{P}^1$ is multiplied by a weighting function $|k|$, an inverse Fourier transformation is performed, which leads to Q. Second, in a process named *back-projection* all the filtered back-projections are added up to obtain $\mu(x,y)$. In figure 3.15, the principle of the filtered back-projection is illustrated.
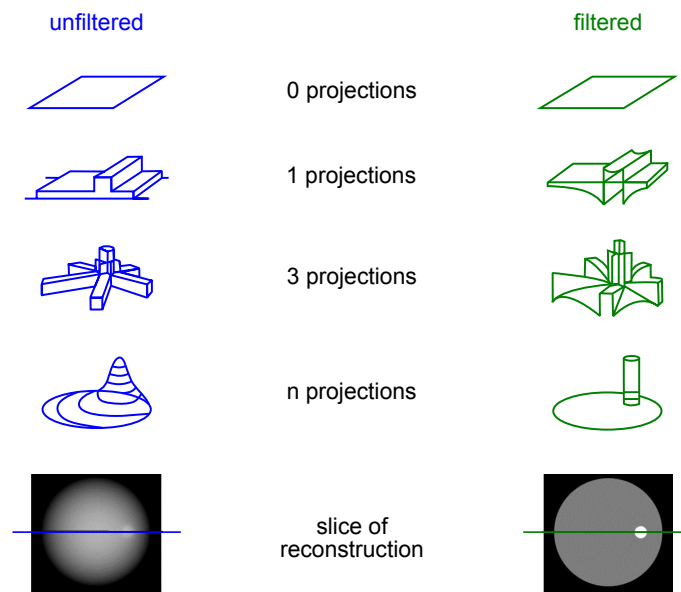
Figure 3.15: Principle of filtered back-projection, adopted from Kalender [2000]. From the top to the bottom, the process to build up the reconstruction is illustrated. Whereas the unfiltered reconstruction in the left column (blue) leads to blurry images, the filtered reconstruction on the right (green) gives corrected results.

Another problem for the practical reconstruction is that the projections cannot be obtained continuously, but in finite discrete steps. The sample interval Δp cor-

responds to the finite size of the pixels. Then, equation 3.9 follows.

$$\Longrightarrow \mu(x,y) \approx \frac{\pi}{A} \sum_{i=1}^{A} \frac{2K}{N} \sum_{m=-\frac{N}{2}}^{+\frac{N}{2}} \mathcal{P}^1\left(\vartheta_i, \frac{2Km}{N}\right) \cdot e^{i\frac{2Km}{N}r} \cdot \underbrace{\left|\frac{2Km}{N}\right| \cdot W}_{=:H}$$

$$= \frac{\pi}{A} \sum_{i=1}^{A} Q(\vartheta_i, r) \tag{3.9}$$

with $N \,\hat{=}\,$ number of pixels in one detector row

$A \,\hat{=}\,$ number of projections

$K = \frac{1}{2\Delta p} \,\hat{=}\,$ highest frequency in the projection[13]

$i \ = 1, ..., A \,\hat{=}\,$ projection numbers for the different angles

$m = -\frac{N}{2}, ..., \frac{N}{2} \,\hat{=}\,$ pixel numbers in a row

$W = \begin{cases} 1, & \text{if } \left|\frac{2Km}{N}\right| \leq K \\ 0, & \text{otherwise} \end{cases}$

Here, H represents a band limited filter function depending on the window function W. There are different types of filter functions, explicitly given in equations 3.10 and 3.11. The most important ones are illustrated in figure 3.16 and are named *Ram-Lak filter H_{RL}* and *Shepp-Logan filter H_{SL}*.
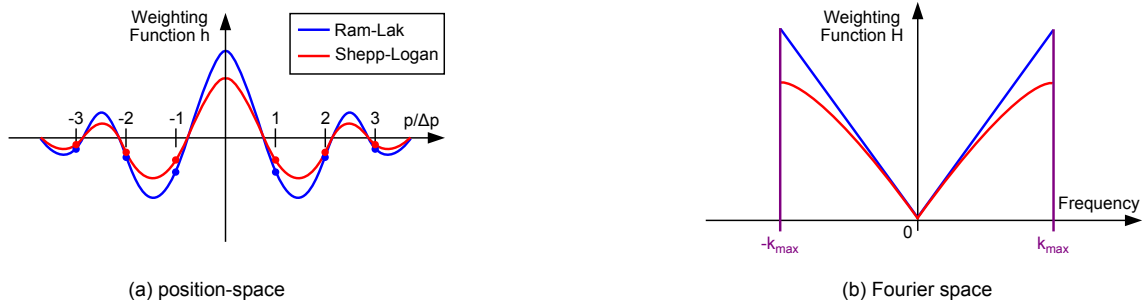
Figure 3.16: Different weighting functions for filtered back-projection. The Shepp-Logan filter suppresses high frequencies, in contrast to the Ram-Lak filter. While H represents the filter in the Fourier space, the convolution kernel in position-space is described by h. A scanning at the sampling points $p = n \cdot \triangle p$ leads to the discrete version $\mathcal{F}^1[H_{SL}(s \cdot \Delta p)]$ [Schlegel and Bille, 2002].

---

[13]if the *Nyquist Theorem* is fulfilled to prevent aliasing (see [Schlegel and Bille, 2002])

$$H_{RL} = \left| \frac{2Km}{N} \right| \cdot W\left(\frac{2Km}{N} \right)$$

$$\Longrightarrow \mathcal{F}^1[H_{RL}(s \cdot \Delta p)] = \begin{cases} \frac{1}{4 \cdot \Delta p}, & \text{if } s = 0 \\ 0, & \text{if } s = \text{even} \\ -\frac{1}{s^2 \pi^2 \Delta p^2}, & \text{if } s = \text{odd} \end{cases} \tag{3.10}$$

$$H_{SL} = \left| \frac{2Km}{N} \right| \cdot \left| \frac{sin\left(\frac{2Km}{N} \right)}{\pi \cdot \frac{2Km}{N}} \right| \cdot W\left(\frac{2Km}{N} \right)$$

$$\Longrightarrow \mathcal{F}^1[H_{SL}(s \cdot \Delta p)] = -\frac{2}{\pi^2 \Delta p^2 \cdot (4s^2 - 1)} \tag{3.11}$$

While H_{RL} is called a ramp filter because of its straight shape, H_{SL} weighs high frequencies less strongly. This can be important for noise reduction since high frequencies mostly represent noise [Schlegel and Bille, 2002; Jähne, 2005; Kak and Slaney, 2001].

4 Results & Discussion

In this chapter, the results of this master thesis are presented and discussed. Monte Carlo simulations are used to determine the X-ray tube output quantitatively. In further sections, different saturation effects of the Medipix detectors as well as image artefacts are described. Furthermore, the influence of the detector settings are investigated. The last section presents CT images under high photon fluxes and compares them to images from previous studies.

4.1 Monte Carlo Simulations

Monte Carlo experiments rely on repeated random sampling from probability distributions and can be used to simulateradiation transport processes. A Monte Carlo simulation based on the EGSnrc code system [Kawkarow, 2000] and the BEAMnrc user code [Kawkarow, 2004] in version V4 2.3.2 was used to convert the X-ray tube currents to the photon fluxes reaching the detector. In addition to the photon flux, also the mean energy and the spectrum were determined.
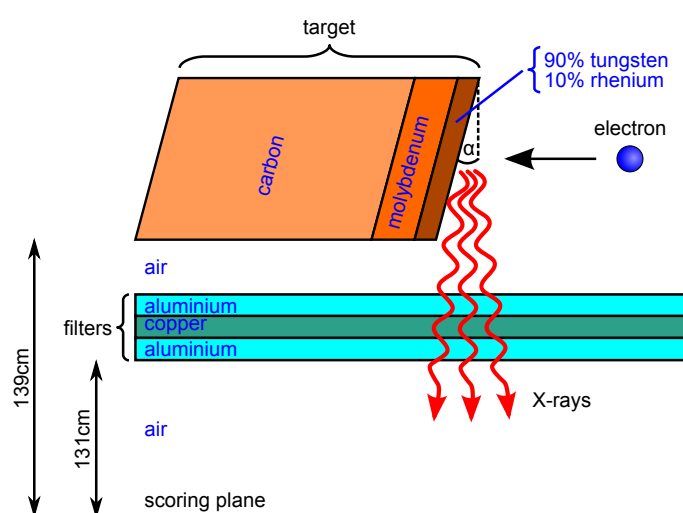
Figure 4.1: Sketch of the setup for the Monte Carlo simulation. A simulated electron is scattered at the target and produces X-rays. In direction of the scoring plane these X-rays are filtered. The scale is adapted for a better visualisation.

4.1.1 Simulation Setup

The geometry for the Monte Carlo simulation is illustrated in figure 4.1. After the simulated electrons are scattered at the target of the X-ray tube, the produced photons are filtered. The target can be separated into three different parts. The first features a 1.5 mm layer of 90 % tungsten and 10 % rhenium (Re). The second is made of molybdenum (Mo) with a thickness of 10 mm, but only a few of the simulated electrons are able to reach this part. The final layer consists of carbon (C). The first filter is made of aluminium (Al) with a thickness of 2.59 mm. The following two filters correspond to the oil of the X-ray tube's cooling tank and can be simulated with layers of 0.1 mm copper (Cu) and 0.2 mm aluminium. The anode angle α is set to $8.5°$ and was determined by the MV-CT (see subsection 4.1.3) [Zuber, 2012].

4.1.2 Simulation Results

In the calculation the X-ray tube is simulated with idealised material properties and $7 \cdot 10^9$ electron histories. The simulated electrons generate X-rays when they are scattered at the anode (section 2.1). These photons may experience photoelectric absorption and Compton scattering on their way to the scoring plane. In table 4.1, the results for several tube voltages are listed.

U_{tube} $[kVp]$	$\overline{E}$ $[keV]$	$\frac{\Phi}{e}$ $\left[\frac{10^{-9}}{cm^2}\right]$	Φ $\left[\frac{10^5}{mA\,s\,mm^2}\right]$	$\frac{\#_\gamma}{Pixel}$ $\left[\frac{10^3}{mA\,s}\right]$	$\frac{\#_{\gamma,exp}}{Pixel}$ $\left[\frac{10^3}{mA\,s}\right]$	Ψ_γ	Ψ_m	$\Delta\Psi$
40	30.9	0.51	0.32	0.87	0.68	0.78	1.10	**0.29**
50	35.9	1.51	0.94	2.56	2.38	0.93	1.16	**0.20**
60	40.5	3.15	1.96	5.35	5.29	0.99	1.21	**0.18**
70	44.5	5.19	3.24	8.82	9.27	1.05	1.25	**0.16**
80	48.2	7.65	4.77	13.0	14.3	1.10	1.29	**0.14**
90	51.6	10.7	6.70	18.2	20.1	1.10	1.33	**0.17**
100	54.8	13.9	8.66	23.6	26.3	1.11	1.35	**0.18**
110	57.6	17.4	10.8	29.5	32.4	1.10	1.38	**0.20**
120	60.1	21.1	13.2	35.9	38.5	1.07	1.40	**0.23**

Table 4.1: Parameters obtained by Monte Carlo simulations. The experimental values and the conversion to pixels are determined for a pixel pitch of 165 μm. The row marked yellow indicates the values obtained for 70 kVp, which is the setting used throughout most of this thesis. The values marked green denote the conversion factors used for several figures.

with U_{tube} = tube voltage
   Φ = photon flux
   e = $1{,}602 \cdot 10^{-19}\,\text{As}$
   $\#_\gamma$ = photon counts

$$\#_{\gamma,exp} = \text{experimental determined photon counts}$$
$$\Psi_\gamma = \left(\frac{\#_{\gamma,exp}}{\#_\gamma}\right)$$
$$\Psi_m = <m> \left(1 - e^{-x\frac{\mu}{\rho}\rho}\right)$$
$$m(\overline{E}) = \text{multiplicity}$$
$$x = 0,1\,\text{cm sensor thickness}$$
$$\frac{\mu(\overline{E})}{\rho} = \text{absorption coefficient of CdTe}$$
$$\rho = 6,2\,\frac{\text{g}}{\text{cm}^3}\,\text{density of CdTe}$$
$$\Delta\Psi = \frac{\Psi_\gamma}{\Psi_m}$$

In order to determine Ψ_m the absorption coefficients for tungsten at different energies have to be obtained[14]. The multiplicity values are interpolated from earlier measurements, which were described in detail by Koenig [2011 a]. This leads to the assumption that the photon fluxes obtained at 70 kVp may be too high by a factor of up to 1.2 due to an incomplete specification of the applied X-ray tube.

In figure 4.2, different spectra obtained by the Monte Carlo simulation are shown. The characteristic X-ray peaks of tungsten can be seen when the electric energy crosses the K-edge at about 70 keV (table 2.1).
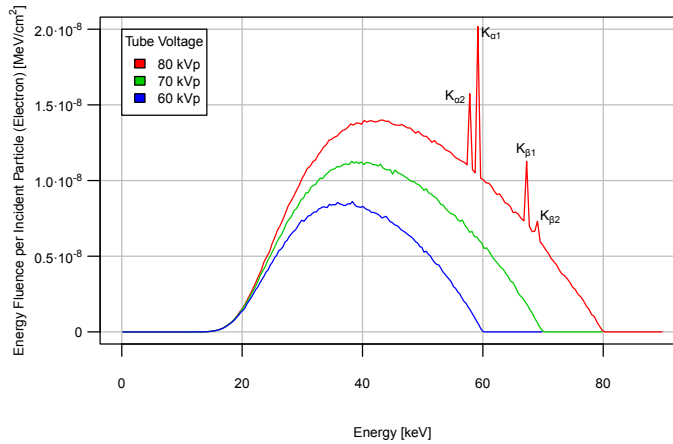
Figure 4.2: Energy spectra at different tube voltages calculated by Monte Carlo simulations.

4.1.3 Sources of Error

The Monte Carlo simulations are subject to systematic errors due to an insufficient knowledge of the X-ray tube's inner structure. In order to minimise these errors,

---

[14]mass attenuation coefficients obtained from the National Institute of Standards and Technology (NIST) [Online; accessed 20-October-2012]:
http://www.nist.gov/pml/data/xraycoef/index.cfm

an MV-CT was performed, as illustrated in figure 4.3. The image was obtained by a linear accelerator, Siemens Artiste. For the simulation the required distances and angles were measured using this figure.
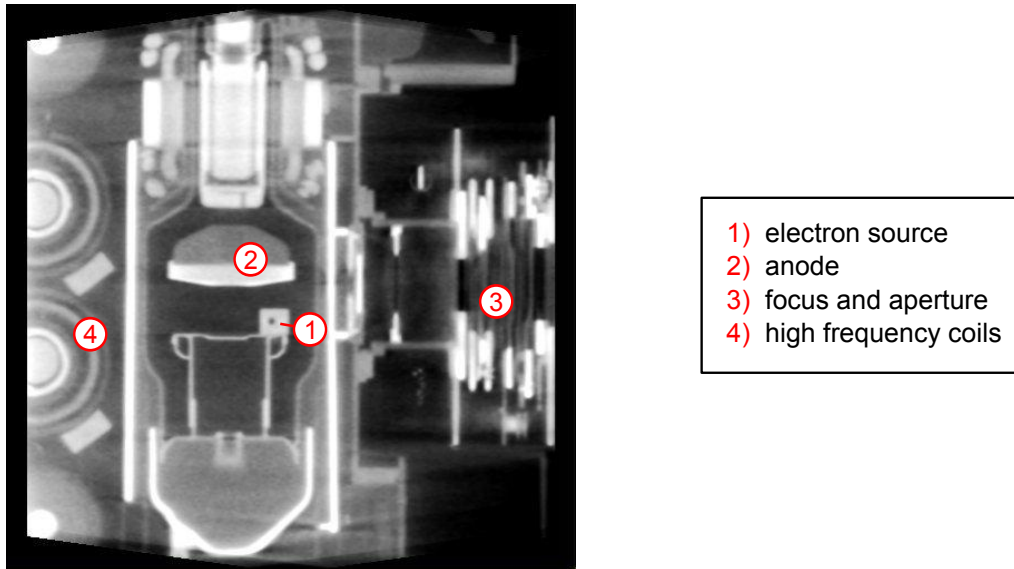
Figure 4.3: Cross sectional MV-CT image of the X-ray tube. In the centre, the accelerated electrons are scattered at the anode and the generated X-rays exit through the aperture on the right. On the left, the transformation coils for the high voltage are visible.

One of the main errors occurs due to the application of the copper and aluminium absorbers. The thicknesses of these filters are obtained from the X-ray tube specifications and are only available for an energy of 100 keV. Furthermore, for the calculation of bremsstrahlung by the electrons a splitting is used. So, instead of a single photon, 2 000 photons are simulated in order to accelerate the calculation. Another error can be caused due to the determination of the distance between tube and detector, which scales with r^2. Also the position at the target where the electrons are scattered is not exactly known. However, the silver coating of the sensor can be neglected since its thickness is only $d_{Ag} \leq 500\,\mathrm{nm}$[15].

4.2 X-Ray Tube Control & Stability

In this section, the X-ray tube control as well as its stability concerning the pulse mode are discussed. These results are used for all of the measurements in the following sections.

---

[15]private communication with Andreas Zwerger (Freiburg Materials Research Center, FMF)

4.2.1 X-Ray Tube Control

A circuit was developed to trigger pulses of the X-ray tube using an RS 232 serial port, as illustrated in figure 4.4. Although it is not possible to achieve shorter imaging times for the applied setup due to a relatively slow moving rotary stage and latencies in the software readout, the simulation of fast projections is possible now.
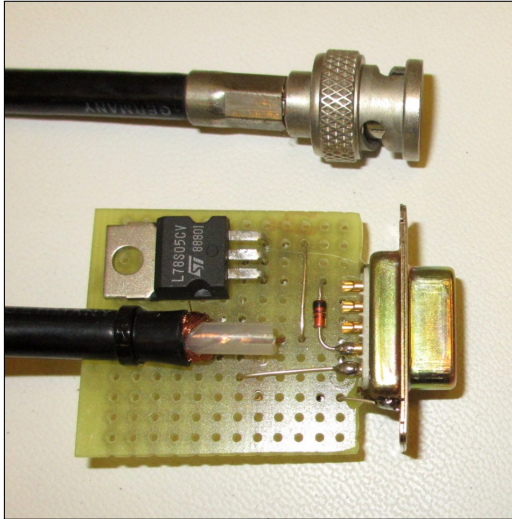
(a) photograph of the device   **(b)** device circuit
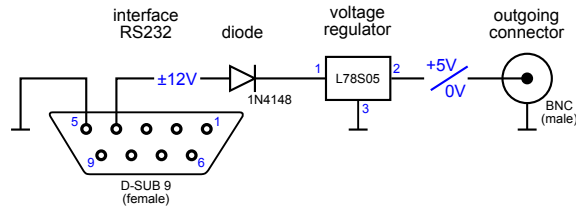
Figure 4.4: Circuit used to trigger X-ray pulses. While the RS 232 incoming connector is linked to the computer, the BNC output connects to the X-ray tube.

The input voltage from the computer is $\pm 12\,\text{V}$ for pulsing and stopping. At the output, a voltage of $+5\,\text{V}$ for pulsing and $0\,\text{V}$ for stopping is presented for the X-ray tube. A silicon diode[16] 1N4148 is used to block the negative voltage and a voltage regulator[17] L78S05 restricts the positive voltage to $5\,\text{V}$. The two capacitors, as requested in the data sheet for stabilising the voltage regulator, are neglected because of low currents in this case.

4.2.2 X-Ray Tube Stability

In this subsection, the control and stability of the X-ray tube is discussed. The detector stability, i.e. the temporal drift of the pixel equalisation and the energy thresholds, has already been discussed in previous studies [Schuebel, 2012]. This leads to an error in all of the measurements and especially in the CT projections. Further information can be found in Koenig [2011 a] or Schulze [2011].

---

[16]data sheet of the diode [Online; accessed 20-October-2012]:
http://www.nxp.com/documents/data_sheet/1N4148_1N4448.pdf
[17]data sheet of the voltage regulator [Online; accessed 20-October-2012]:
http://www.datasheetcatalog.org/datasheet/stmicroelectronics/2148.pdf

Pulse Widths Deviations

As mentioned in the previous sections, the measurements with the X-ray tube are carried out in fluoroscopic mode $(0 - 10\,\mathrm{mA})$ and in pulse mode $(10 - 250\,\mathrm{mA})$ to cover a wide range of tube currents and photon fluxes. However, the choice of the acquisition times also depends on the mode. In both modes, a preferably long time should be chosen to obtain a good SNR. The upper limit is given by the maximum count rate of the detector, which is $11\,810$ (see section 3.1.3). This is the reason why the acquisition time varies for different tube currents.

While in fluoroscopic mode the choice of the acquisition time is not limited to a low threshold, in pulse mode the choice is restricted by the X-ray tube stability, as illustrated in figure 4.5. Since the X-ray tube is emitting irregular pulses at low pulse widths, a pulse width of at least $20\,\mathrm{ms}$ is chosen for all of the measurements.
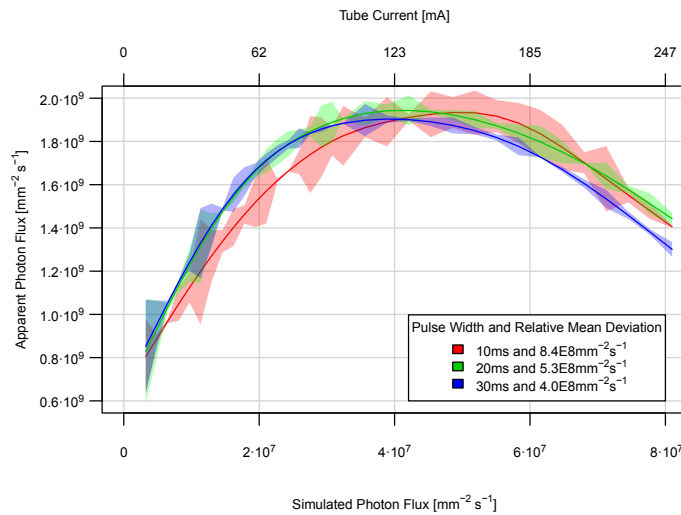
Figure 4.5: Count rate versus photon flux for different pulse widths and a pixel pitch of $165\,\mathrm{\mu m}$. The I_{Krum} value was set to 20 and the values are smoothed. The light areas indicate the measurement deviations which are given by the difference between the measured value and the corresponding smoothing spline. Note that these deviations are reduced for larger pulse widths.

X-Ray Tube Log File Compensation

Another investigation is made to compensate the irregularity between fluoroscopic and pulse mode, as illustrated in figure 4.6. Since the measurement data of the pulse mode are usually shifted to higher count rates due to shorter pulse widths than adjusted, the so called Log File tables of the X-ray tube are considered for compensation. Log Files contain the values of the internal measured tube currents as well as the pulse widths of the X-ray tube for every pulse. Therefor the values

are automatically written in a single file after the anode is turned off[18].
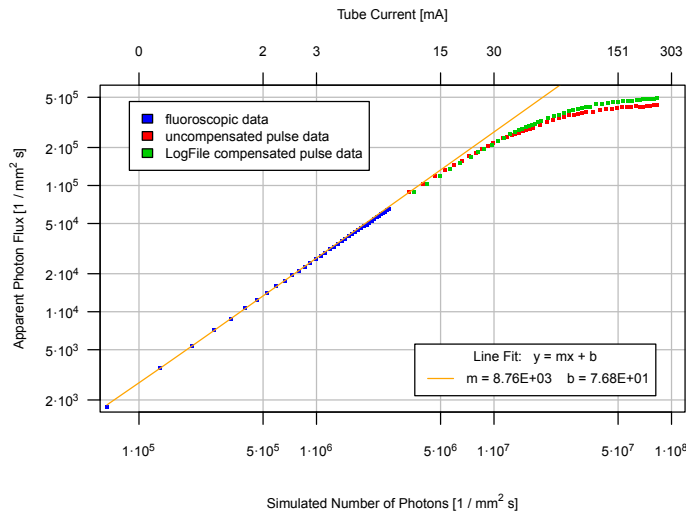
Figure 4.6: Photon flux versus simulated number of photons at an I_{Krum} value of 60, a pulse width of $20\,ms$ and $U_{tube} = 70\,kVp$ in double logarithmic scale. While the data marked red indicate the measurements without pulse width correction, the green dots represent data compensated by the X-ray tube's Log Files. The fitted straight line (orange) corresponds to the first ten measurement values at low photon fluxes where a linear behaviour is assumed.

Since I_{tube} is different for each pulse measurement, it is not possible to perform several measurements in order to determine a standard mean and error. As additionally the pulse width changes, the mean values are replaced by the weighted mean counts $\overline{N}$ and the weighted mean currents $\overline{I}$, as shown in the equations 4.1.

$$\overline{N} = \frac{\sum_i I_i N_i}{\sum_j I_j} \qquad \text{and} \qquad \overline{I} = \frac{\sum_i I_i N_i}{\sum_j N_j} \tag{4.1}$$

4.3 Saturation Effects

Here, saturation effects are examined to estimate the maximum possible photon flux at various detector settings for the use in CT imaging. Detector DACs are varied to discuss their influence. Especially the DAC I_{Krum}, which shapes the discharge current of each pixel's charge sensitive preamplifier and controls the leakage current compensation, is important for these examinations. This is because the I_{Krum} values change the impact of pile-up effects in the detector, but do not influence other saturation effects, as e. g. polarisation.

---

[18]implemented by Dr. Simeon Nill (DKFZ)

For all measurements described in this subsection, the pulse width is set to 20 ms and the acceleration voltage of the X-ray tube to 70 kVp, corresponding to a mean photon energy of 44 keV. The photon flux, which is estimated by Monte Carlo simulations, may contain an error of 16 % (chapter 4.1). All measurements are performed using just a lower energy threshold of 10 keV to avoid background noise and to use the whole spectrum of the X-ray tube, as can be compared in figure 4.2.

The count rate depends on the photon flux and on the setting of the I_{Krum} DAC. In figure 4.7, it can be seen that the critical photon flux, at which the detector's linear response breaks down, can be shifted towards higher values by increasing this current, which corresponds to reducing the pulse shaping time.
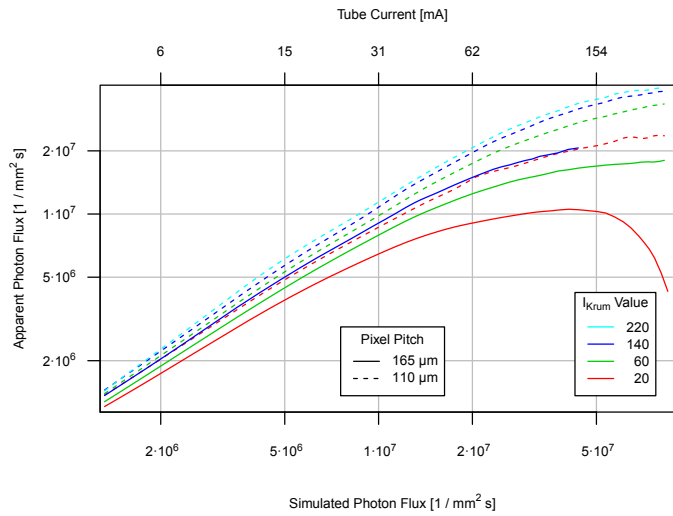
Figure 4.7: Count rate versus photon flux for various I_{Krum} values and two different pixel pitches at a low energy threshold of 10 keV, represented in double logarithmic scale. The photon flux is estimated by Monte Carlo simulations and is subject to an error of 20 % [Rink et al., 2012].

In comparison, the curves at a lower pixel pitch are shifted to higher photon fluxes since more charge sharing between the pixels occur at a relatively low THL value. Additionally, the curves for a smaller pixel pitch as well as higher I_{Krum} values are more linear due to less pile-up effects (figure 2.11). It should also be noticed that the smaller pixel pitch profits less from higher I_{Krum} values. This is found by comparing measurements for I_{Krum} values larger than 140. While the linearity at the pixel pitch of 165 μm continues to profit, it does not for the smaller pixel pitch. Consequently, the count rates may already be limited by sensor polarisation in this latter case [Rink et al., 2012].

It could be verified by a DAC DelayN scan that the observed saturation does not occur due to a digital pile-up effect since the scan supplies a constant value depending on the other settings of the measurement. The DAC DelayN controls the output pulse width at the digital part of the ASIC.

For most applications, a quantity, which is more critical than the position of this maximum, is the position where the count rate starts to deviate notably from the otherwise linear dependence on the incoming photon flux. For a deviation of 10 % or higher from the linear behaviour, this is shown for single pixels in terms of a pixel map in figure 4.8. To obtain these values the measured data is compared to a fitted straight line, taking into account the first five values of each measurement since a linear beaviour of the detector is assumed for low photon fluxes.
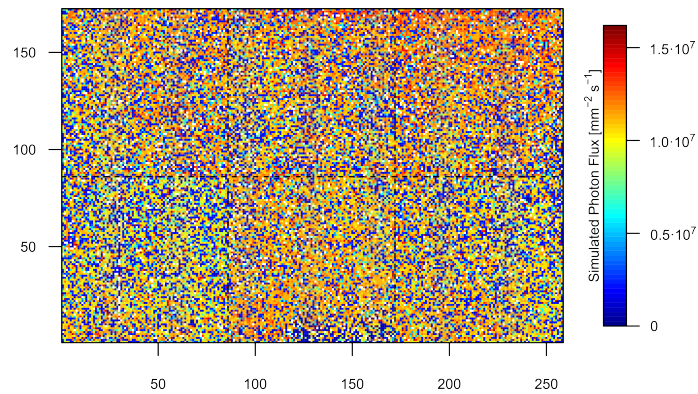
Figure 4.8: Pixel map of the tube current at an I_{Krum} value of 100 for which a deviation of at least 10 % from the ideal linear response occurs. A pixel pitch of 165 μm is used.
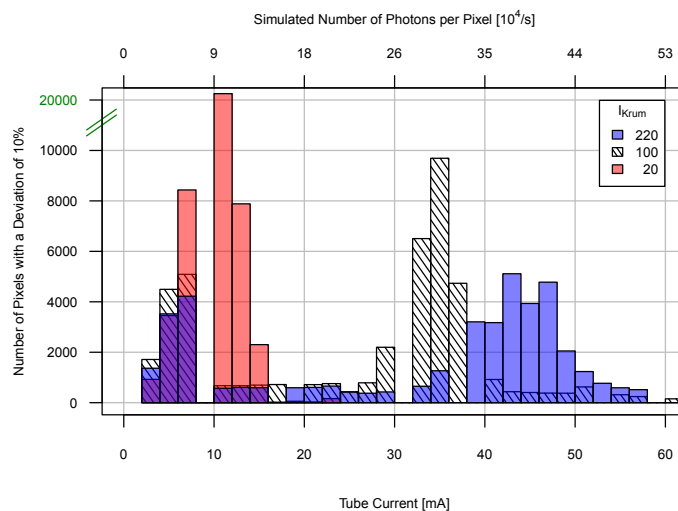
Figure 4.9: Number of pixels with a deviation of 10 % from an ideal linear response versus tube current. The pixel pitch used for these measurements is 165 μm. Note that the scale of the y-axis is broken between values of 10 000 and 20 000, marked in green.

In histogram 4.9, the number of pixels, which deviate by 10 % or more from a linear response, are shown as a function of the tube current. The missing measurement values of the tube currents I_{tube} between 8 and 10 mA is due to the different operation modes of the X-ray tube (see section 3.1.1). In fluoroscopic mode, the X-ray tube can be safely operated up to a power of 550 mW, which is reached at $I_{tube} > 7.8$ mA and $U_{tube} = 70$ kVp. The increase of the number of deviating pixels before this measurement gap is supposed to be of the same origin. Another important aspect can be seen by comparing the number of pixels of the different I_{Krum} measurements. The maxima for higher I_{Krum} values is lower and the difference of the number of pixels to neighbouring measurement values with the same I_{Krum} is reduced. The reason for these effects is that the probability of measurement errors is increased when the deviation starts to request at low photon fluxes. The maximal values are shown in table 4.2 for both pixel pitches and deviations of 5 and 10 %.

maximum	110 µm		165 µm	
deviation	$I_{Krum} = 20$	$I_{Krum} = 140$	$I_{Krum} = 20$	$I_{Krum} = 140$
5 %	0.9	1.4	0.2	1.0
10 %	1.1	2.3	0.4	1.3

Table 4.2: Critical photon fluxes for which a deviation from the detector's linear response of more than 5 or 10 % occurs, averaged over all the pixels of a single chip. The values given are in units of 10^7 mm^{-2} s^{-1} [Koenig et al., 2012].

While increasing the I_{Krum} DAC value allows to extend the linear range of the measured count rates, it implies a higher ENC of the detector. However, the energy
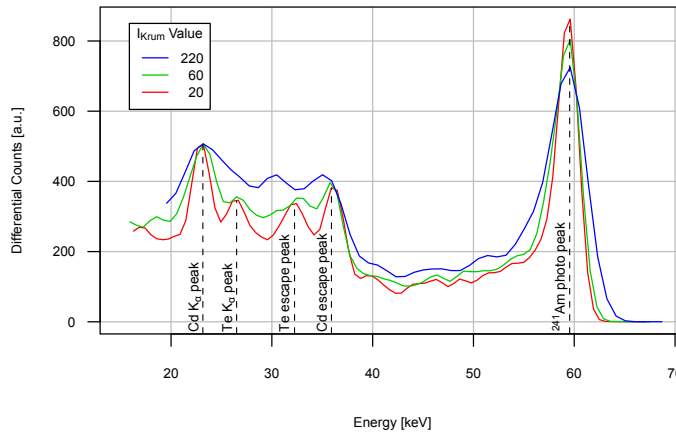
Figure 4.10: Energy response functions for different I_{Krum} values and a pixel pitch of 165 µm, normalised to the Cd K_α peak at 23.2 keV for a single pixel [Rink et al., 2012].

response function is affected only moderately, as illustrated in figures 4.10 and 4.11. In these measurements the americium source was used.
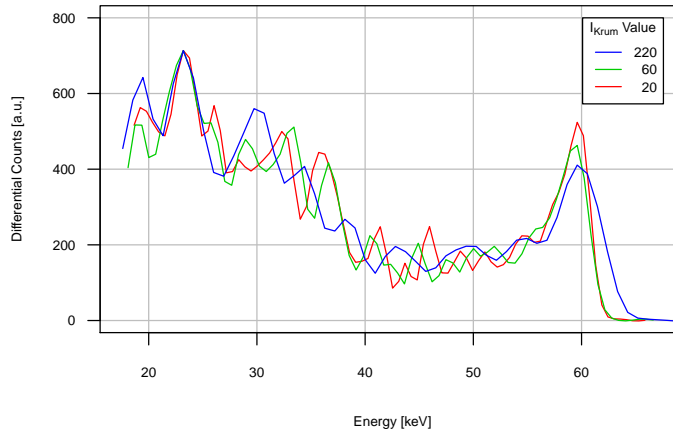
Figure 4.11: As figure 4.10, but for a pixel pitch of 110 μm.

4.4 Image Inhomogeneities & Non-Counting Pixels

Saturation effects lead to image artefacts aligned parallel to one chip side across the detector. These artefacts are visible as horizontal stripes coloured yellow in figure 4.12 b. This can be induced by varying I_{Krum} currents caused by wafer inhomogeneities. As these artefacts end at chip borders, they cannot be caused by the CdTe sensor, but must be due to detector readout.

Furthermore, two different types of non-counting pixels can be observed: First, bulk defects appear always at the same position on the detector and are found to decrease in size with higher I_{Krum} values, illustrated in figure 4.13. This is likely due to increased leakage currents in the sensor areas pertaining to these sites. They can be compensated for more efficiently with higher I_{Krum} values.
Second, non-counting pixels randomly appear at different positions during each measurement. The number of these non-counting single pixels increases with higher photon fluxes and can be counter-acted by higher I_{Krum} values, as shown in figure 4.14. Another important factor in this analysis is the energy threshold. In the flatfield images 4.12 b and c, which were obtained at a low discriminator setting of 10 keV, numbers of approximately 2 100 and 1 700 non-counting single pixels occur. The measurements illustrated in figure 4.14 at 65 keV exhibit lower numbers at the same photon flux. These defects appear not to be caused by sensor polarisation since their number rises constantly with a higher bias voltage. An explanation might

a) $\Phi = 3 \cdot 10^5 \frac{1}{mm^2 s}$,   b) $\Phi = 3 \cdot 10^7 \frac{1}{mm^2 s}$,   c) $\Phi = 3 \cdot 10^7 \frac{1}{mm^2 s}$,
$I_{Krum} = 20$ $I_{Krum} = 20$ $I_{Krum} = 100$
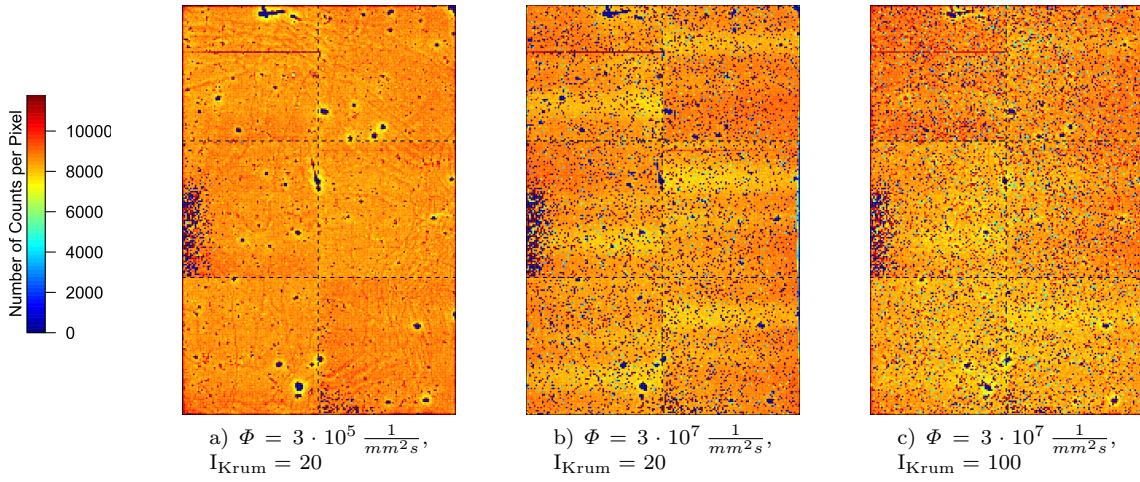
Figure 4.12: Detector flatfield images at different I_{Krum} values and photon fluxes Φ at an energy threshold of 10 keV. The scale of the photon counts in b and c is adjusted for a better comparison [Rink et al., 2012].

be leakage current instabilities in single pixels, which lead to a voltage at the low discriminator input permanently exceeding its threshold, as sketched in figure 4.15.
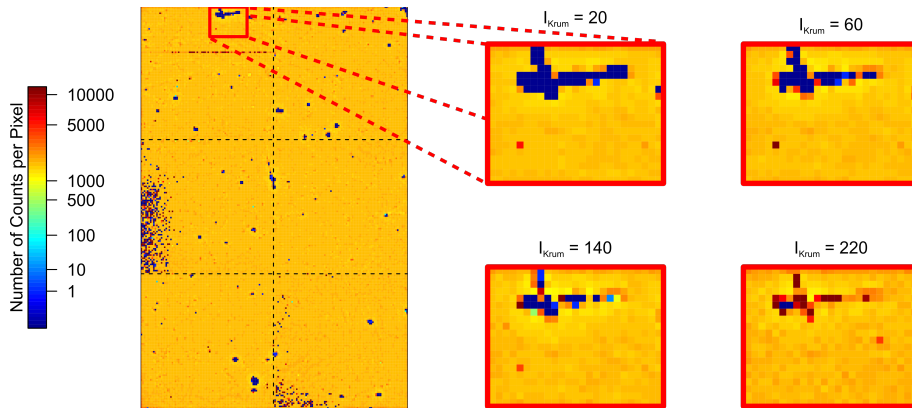
Figure 4.13: On the left, a flatfield image obtained at an I_{Krum} value of 20 is shown. The bulk of non-counting pixels in this flatfield image marked with the red box is indicated in more detail on the right at four different I_{Krum} settings. The non-counting detector areas shrink with a more efficient leakage current compensation [Rink et al., 2012].

Note that in order to exclude bulk defects from this analysis, pixels were only included when they showed a count number of zero only once within an interval of three frames. Interestingly, not all the curves shown exhibit a strictly monotonic behaviour. This effect presently cannot be explained but was ensured not to be caused by an interpolation artefact. The decrease of the red solid line ($I_{Krum} = 20$,
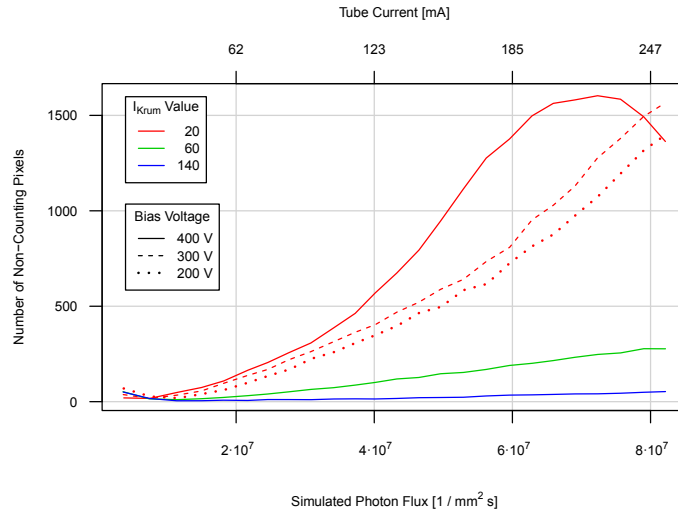
Figure 4.14: Number of non-counting single pixels versus photon flux for a pixel pitch of 165 µm and different I_{Krum} values as well as bias voltages. The low energy threshold was set to 65 keV [Rink et al., 2012].

$U_{Bias} = 400$ V) at high photon fluxes is due to the image inhomogeneities mentioned earlier [Rink et al., 2012].
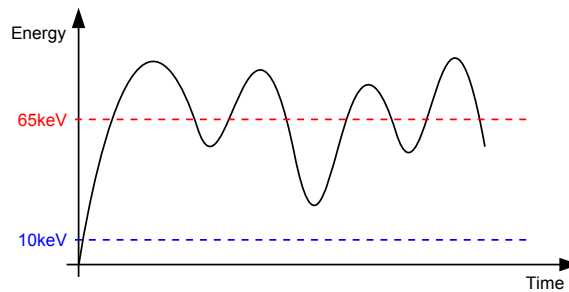
Figure 4.15: Explanation of the different numbers of non-counting pixels for various low energy thresholds. Whereas the threshold at 65 keV can register most of the signals, the threshold at 10 keV is permanently below the measured data.

4.5 Estimation of the Detrapping Time

The detrapping time τ_D depends on several trap effects and is insufficiently known in literature. These kind of effects are caused by impurities in the crystal, which produce trapping levels between the valence and the conduction band. When charges are trapped, they do not contribute to the conductivity of the semiconductor.
By means of Monte Carlo simulations (section 4.1) and the measurements shown in figure 4.16, it is possible to give an upper bound of the detrapping time. While a higher tube voltage shifts the maximum photon flux to a lower tube current, a

higher bias voltage shifts the maximum to higher values. This is also justified in equation 4.2, where ϕ_y^* indicates the maximum photon flux [Bale and Szeles, 2008].
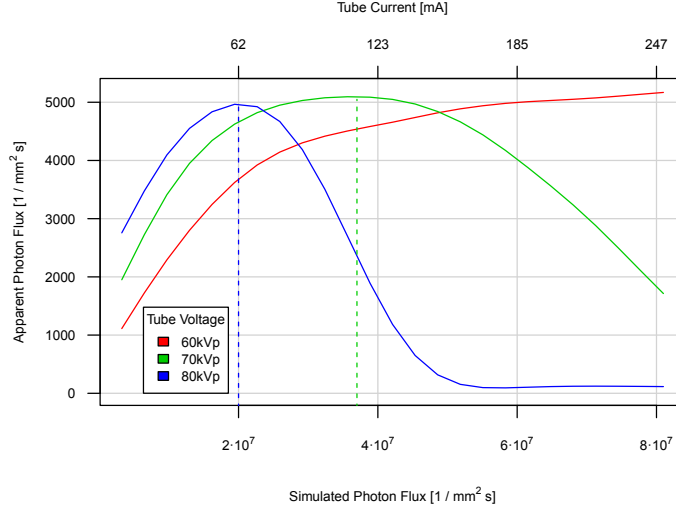
Figure 4.16: Count rate versus photon flux for a pixel pitch of 165 μm and various tube voltages U_{tube}. The I_{Krum} value was set to 220. The maxima are indicated by dotted lines.

$$\phi_y^* = \frac{\varepsilon_0 W U_{bias}^2}{qL\overline{E}_\gamma \Lambda^2}\left(\beta - \frac{L}{\Lambda}e^{\frac{-L}{\Lambda}}\right)^{-1}\frac{\mu_h\tau_h}{\tau_h + \tau_D}$$

$$\Longleftrightarrow \tau_D = \frac{\varepsilon_0 W U_{bias}^2}{qL\overline{E}_\gamma \Lambda^2}\left(\beta - \frac{L}{\Lambda}e^{\frac{-L}{\Lambda}}\right)^{-1}\frac{\mu_h\tau_h}{\phi_y^*} - \tau_h$$

$$(4.2)$$

with $\begin{aligned}
\varepsilon_0 &= 8{,}854\cdot 10^{-12} &&\widehat{=}\text{ dielectric constant}\\
W &= 4{,}43\,\text{eV} &&\widehat{=}\text{ mean energy to generate an electron hole pair}\\
U_{bias} &= -400\,\text{V} &&\widehat{=}\text{ bias voltage}\\
q &= 1{,}602\cdot 10^{-19}\,\text{C} &&\widehat{=}\text{ charge}\\
L &= 1\,\text{mm} &&\widehat{=}\text{ detector thickness}\\
\beta &= 1 - e^{\frac{-L}{\Lambda}}\\
\mu_h\tau_h &= 0{,}75\cdot 10^{-4}\,\frac{\text{cm}^2}{\text{V}} &&\widehat{=}\text{ mobility-lifetime product}\\
\tau_h &= 2\cdot 10^{-6}\,\text{s} &&\widehat{=}\text{ hole lifetime}
\end{aligned}$

The mean photon energy $\overline{E}_\gamma(70\,\text{kVp}) = 44{,}2\,\text{keV}$ is obtained by Monte Carlo simulations (see table 4.1). The mean free path length is determined by $\Lambda(\overline{E}_\gamma) = \frac{1}{\mu(\overline{E}_\gamma)} = 8{,}4\cdot 10^{-5}\,\text{m}$, where μ indicates the linear attenuation coefficient. Furthermore, $\beta = 1 - e^{\frac{-L}{\Lambda}}$.

An upper limit for the detrapping time is estimated by including the value for the maximum photon flux $\phi_y^*(70\,\text{kVp}) \approx 3{,}2\cdot 10^{13}\,\text{m}^{-2}\text{s}^{-1}$, which is extracted from figure

4.16. A requirement for this extraction is that the measurement at higher I_{Krum} values only contain little pile-up. Since pile-up could not be avoided completely, an upper limit is estimated in equation 4.3:

$$\Longrightarrow \tau_D(70\,\mathrm{kVp}) \lesssim 3{,}0 \cdot 10^{-2}\,\mathrm{s}. \tag{4.3}$$

4.6 CT Imaging at High Photon Fluxes

This section describes the process to acquire and correct CT images under high photon fluxes. Furthermore, these high flux images are compared to low flux images. Therefor a circuit was developed for the X-ray tube control to achieve a faster signal pulse rate.

4.6.1 Restoring Linearity

Saturation effects are discussed in section 4.3. However, figure 4.7 hides the fact that not each pixel shows the same count rate limitations. This becomes obvious in figures 4.12, where the inhomogeneities at high photon fluxes are shown. The inhomogeneities cannot be corrected by flatfield images since they depend on the local photon flux. The local photon flux in turn is a function of the thickness and the absorption coefficients of the imaged objects.
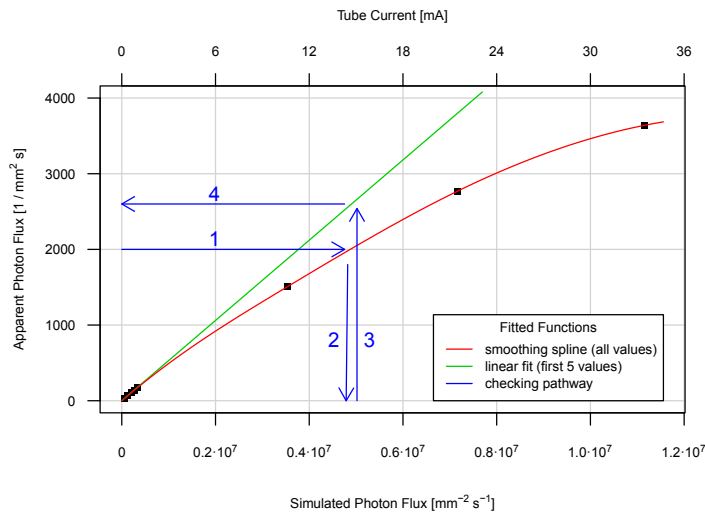
Figure 4.17: Schematic illustration of the CT correction algorithm for a single pixel. The numbers indicate the steps, which have to be performed to acquire a correction curve for a particular pixel.

Nevertheless, the inhomogeneities can be reduced by increasing the I_{Krum} DAC, but due to fluctuations of the count rates the I_{Krum} value should be chosen as small

as possible [Schuebel, 2012]. In order to push limits further a correction algorithm is developed, as illustrated in figure 4.17. The algorithm has to be applied to each pixel in a projection. For this the behaviour of the pixels has to be determined by measuring the count rate for several different photon fluxes and interpolating the missing values by a spline function (curve marked in red). Additionally, a straight line is fitted through the first five measurement values (line marked in green).

Now, it is possible to obtain a pixel's deviation for a given photon flux in the range considered. For this purpose, the simulated number of photons is determined for a measured photon flux, as given by the curve marked in red. The result is used to determine the expected linear photon flux. By dividing these two values a factor for every pixel is calculated, that can be used to correct the inhomogeneities, as illustrated in figure 4.18.
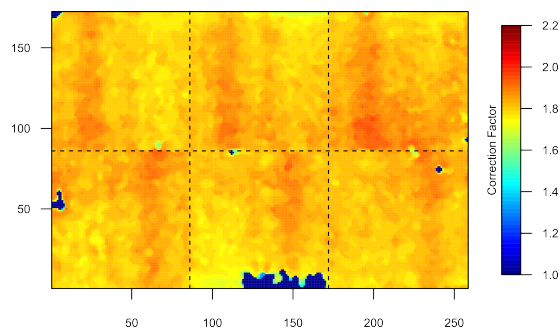
Figure 4.18: Pixel map of the correction factors at an I_{Krum} value of 20, a lower energy threshold of $25\,keV$ and a tube current of $40\,mA$ for a flatfield. A median filter for the eight neighbours of each pixel is used in five iterations to remove outliers.

(a) flatfield image   **(b)** high flux and median correction of (a)
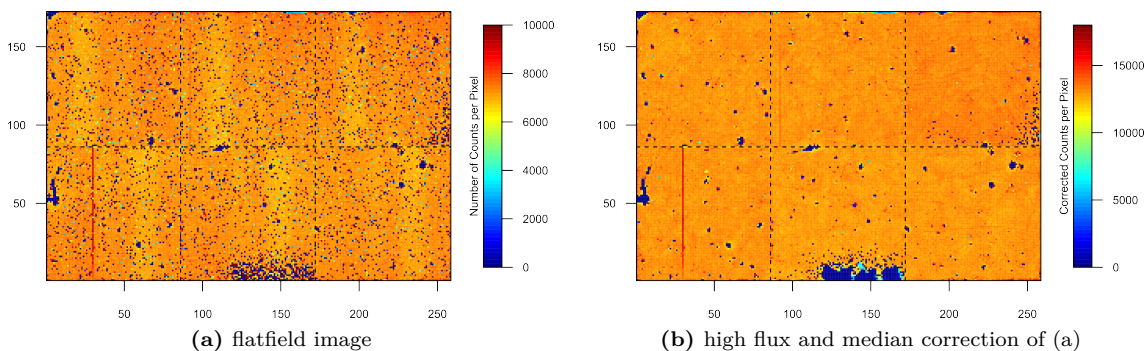
Figure 4.19: High photon flux correction and median of 20 exposures for a flatfield image. The inhomogeneities (vertical yellow stripes) in figure (a) could be completely compensated in (b).

Thus, the count rate measurements from section 4.3 are not only useful to determine the saturation effects or the deviations of each pixel from the linear behaviour

respectively, like in figure 4.8, but also to correct images at high photon fluxes, as shown in figure 4.19.

Several methods are tested to minimise fitting errors. In order to remove outliers in the measured curves, polynomials with three degrees of freedom were fitted. However, since these outliers are limited and the low number of degeres of freedom proved to be insufficient, a smoothing spline is used. For a single projection, 100 smoothing splines corresponding to 100 pixels are shown in figure 4.20. This illustrates the diversity among the pixels.
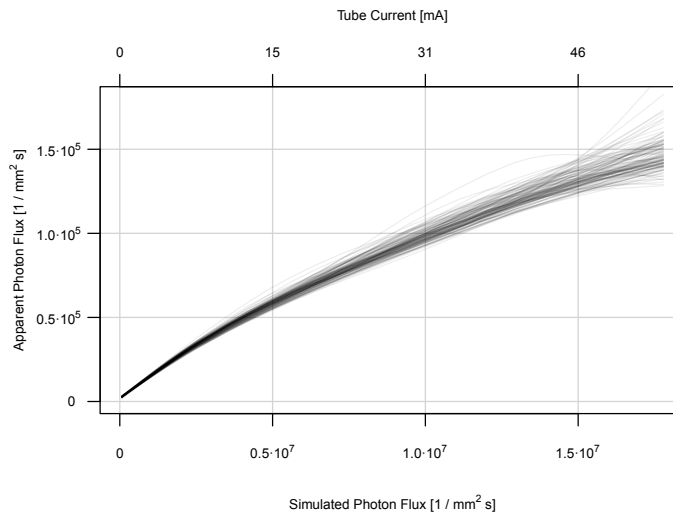
Figure 4.20: Count rate versus photon flux for 100 single pixels of chip 4 for a pixel pitch of 165 µm. The I_{Krum} value was set to 20. A darker colour indicates that several curves coincide.

The correction algorithm was not found to change strongly during a time period of several days. In figure 4.21, two correction matrices are compared, which were measured at different days. Here, the correction factors for each pixel of two flatfields are divided. Afterwards, a Gaussian distribution $f(x) = \frac{c}{\sigma\sqrt{2\pi}} e^{-\frac{1}{2}\left(\frac{x-\mu}{\sigma}\right)^2}$ is fitted to determine the standard deviation. The free parameter c describes an offset of the distribution, σ represents the standard deviation and μ the mean value.

4.6.2 CT Image Reconstruction

To obtain CT images under high photon fluxes several steps have to be performed, as illustrated in figure 4.22.

First, a measurement to determine the pixels' deviation from linearity has to be carried out, as explained in section 4.6.1, in order to correct inhomogeneities. Second, a couple of flatfield images are recorded before the projection images with the phantom can be obtained. The high flux correction for the projection images in
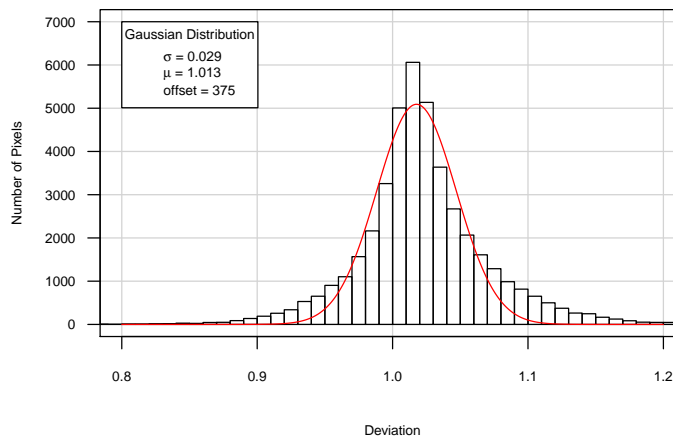
Figure 4.21: Ratio of two correction matrices obtained at a photon flux of $1.3 \cdot 10^7 \, \text{mm}^{-2}\text{s}^{-1}$ ($I_{\text{tube}} = 40 \, \text{mA}$) for a pixel pitch of $165 \, \mu\text{m}$. The I_{Krum} value was set to 20. The curve marked in red indicates a Gaussian.

4.22 b is only implemented for the reconstructed row and its two neighbour rows in order to reduce computation times. The correction of the neighbouring rows is necessary since a median filter is applied afterwards.

Then, all of the flux-corrected projections additionally have to be corrected by flat-field images, the defect correction and median filters. Finally, after filtering the sinogram the back-projection is performed to obtain the reconstructed image.

The color scale in figure 4.22 d represents the reconstructed absorption coefficients in units of cm^{-1}. The ring artefacts are due to adjustment differences between the different chips and energy drifts during the measurement as well as the correction method. The dark blue spot just right to the gadolinium labeling indicates an air bubble, which can arise in a phantom capillary.

The reconstructed absorption coefficients in the CT images are two orders of magnitude smaller than the expected coefficients, which means that more events are detected than there are photon interactions. This is due to a biased energy response function (figures 4.10 and 4.11) and is caused by charge sharing as well as characteristic X-rays.

4.6.3 Hounsfield Calibration

The calibration in Hounsfield Units (HU) is performed by selecting an area in the reconstructed CT image, corresponding to PMMA. The chosen area is always located at the same position, as marked with a red square in figure 4.22 d. Its mean value is set to 0 by the aid of equation 4.4. PMMA is used as reference material here since

(a) single phantom projection

(b) high flux correction of (a) for the required rows

(c) sinogram of all projections

(d) reconstructed CT image
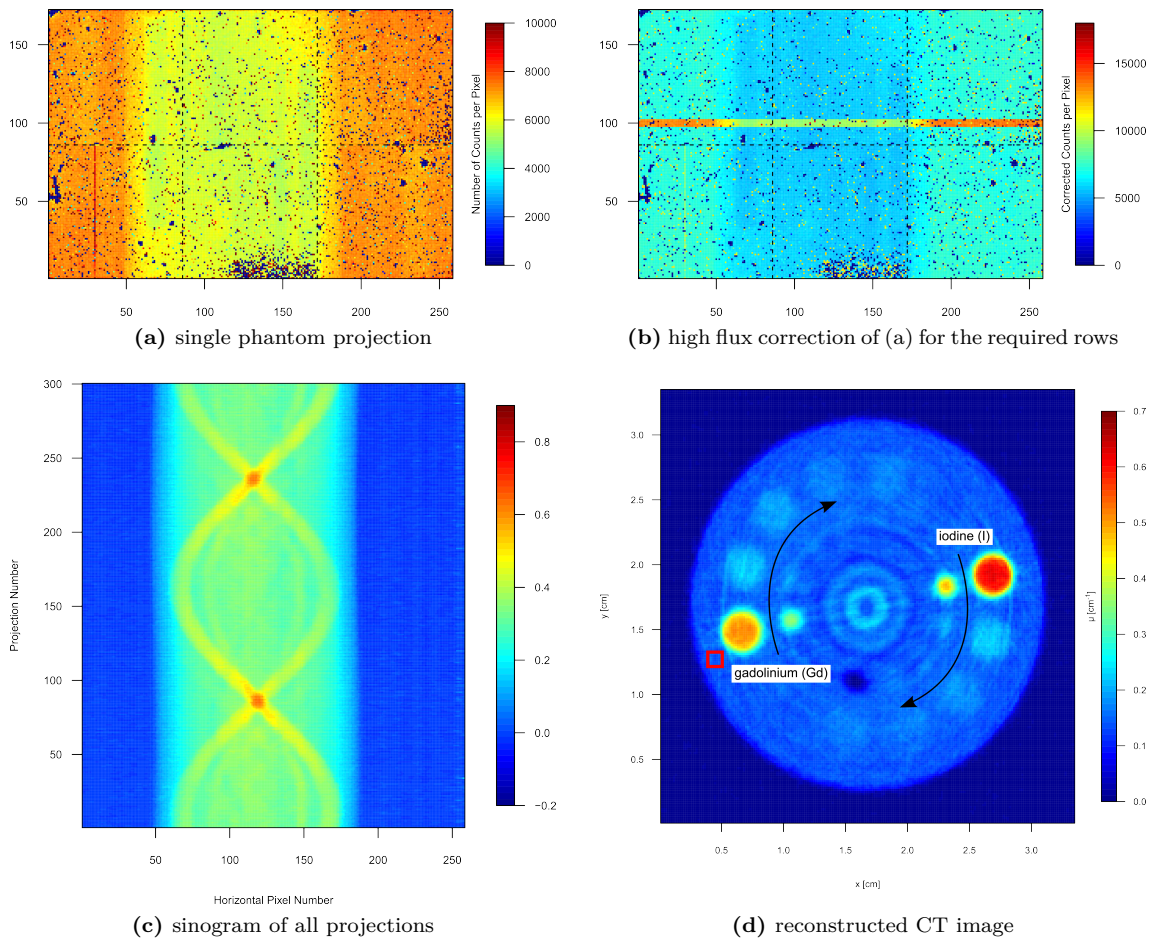
Figure 4.22: CT image reconstruction. Only the 100th row of the projections with the phantom is considered since a 2D reconstruction is performed. The red square in (d) will be used for Hounsfield calibration described in section 4.6.3. The measurements were obtained at an energy threshold of $10\,\text{keV}$. 300 projections were recorded at an angular interval of $360\,^{\circ}$.

it is the dominant material:

$$HU = 1000 \, \frac{\mu_{image} - \mu_{PMMA}}{\mu_{PMMA}}. \tag{4.4}$$

In figure 4.23, CT reconstructions are compared to HU calibrated images. While the correction algorithm is useful to correct the absolute absorption coefficients, it does not change the relative distances between the coefficients. This can be seen by comparing the upper figures 4.23 a-c, where b completely differs, to the bottom figures 4.23 d-f, which are nearly equivalent.

In order to confirm these results, further measurements at $I_{\text{Krum}} = 100$, $U_{\text{tube}} = 100\,\text{kVp}$ and a pulse width of $50\,\text{ms}$ were performed. Additionally, a fast CT was

(a) $\Phi = 1.0 \cdot 10^6 \, \text{mm}^{-2}\text{s}^{-1}$ ($I_{\text{tube}} = 3 \, \text{mA}$)

(b) $\Phi = 1.3 \cdot 10^7 \, \text{mm}^{-2}\text{s}^{-1}$ ($I_{\text{tube}} = 40 \, \text{mA}$)

(c) 40 mA, corrected

(d) data from (a), but in HU

(e) data from (b), but in HU

(f) data from (c), but in HU
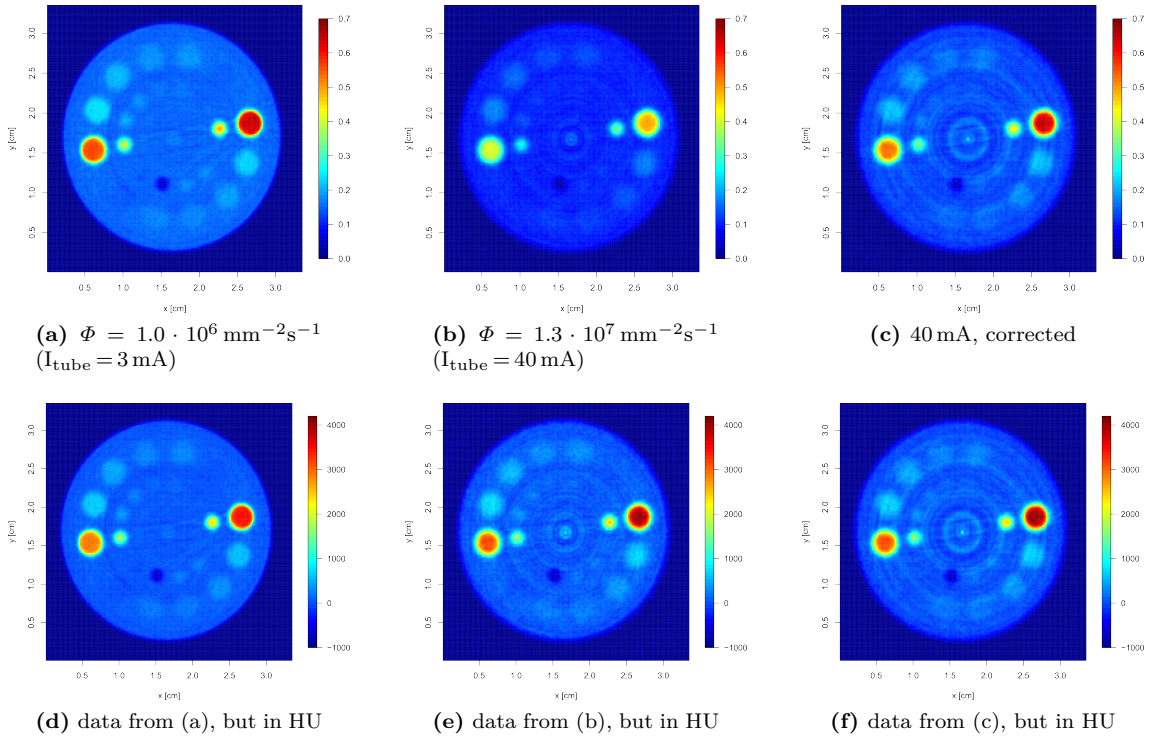
Figure 4.23: CT reconstructions compared to Hounsfield calibrated images. The measurements were obtained at an energy threshold of 25 keV, $I_{\text{Krum}} = 20$, $U_{\text{tube}} = 70 \, \text{kVp}$ and a pulse width of 20 ms. 600 projections were recorded at an angular interval of $360\,^\circ$.

simulated by only recording the 15th pulse of each projection angle with a pulse-to-pulse time of 1 ms. However, all of these measurements lead to similar results.

4.6.4 Contrast Agent Discrimination

The discrimination of photon energies is a crucial aspect to discriminate tissues marked with different contrast agents in a single image. In this section, the separation of two contrast agents at low photon fluxes is shown. Additionally, these results are compared to the studies at high fluxes.

CT Images at various Energy Ranges

In what follows, the reconstruction proceedure is tudied at different energy thresholds. For this purpose the correction curves are recorded at various discriminator settings, as illustrated in figures 4.24 and 4.25. It can be seen that higher energy thresholds lead to lower count rates. Furthermore, the curves obtained at higher thresholds exhibit a lower curvature since the detector is able to count more events. This result is explained by figure 4.26.

Another important point illustrated in figure 4.25 is that curves obtained at energies higher than the mean photon energy of 44.5 keV ($U_{tube} = 70$ kVp, see table 4.1) are bent to higher photon fluxes, in contrast to the expected behaviour.
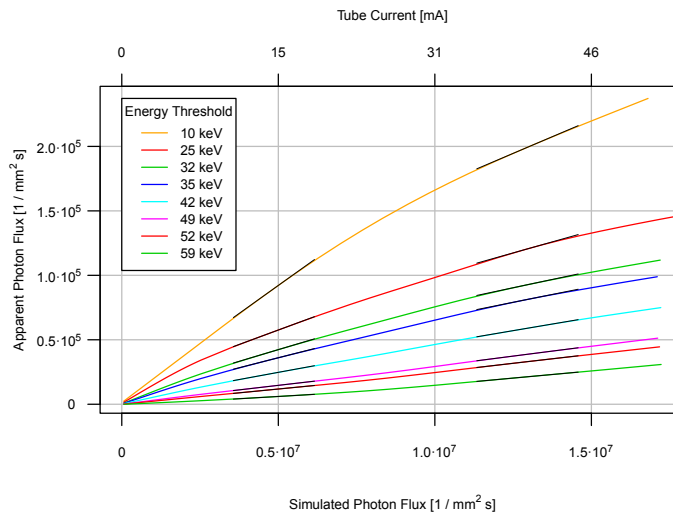
Figure 4.24: Correction algorithm for different energy thresholds. The tangential lines to the curves coloured black indicate the various slopes at $\Phi = 4.9 \cdot 10^6 \, \mathrm{mm}^{-2}\mathrm{s}^{-1}$ ($I_{tube} = 15$ mA) and $\Phi = 1.3 \cdot 10^7 \, \mathrm{mm}^{-2}\mathrm{s}^{-1}$ ($I_{tube} = 40$ mA).
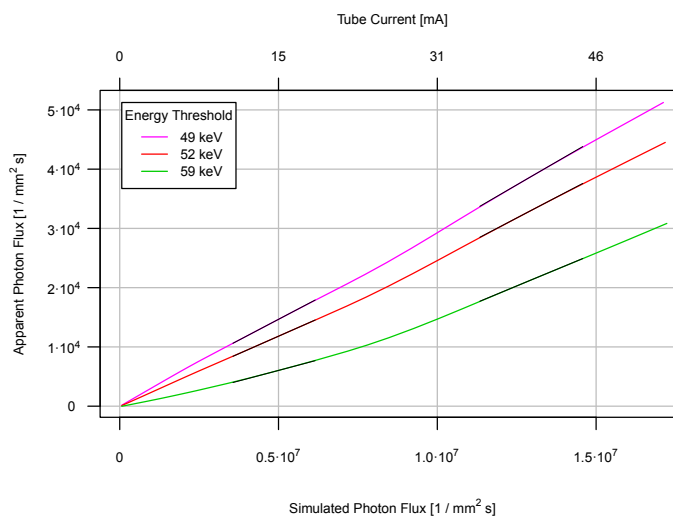
Figure 4.25: As figure 4.24, but with different scaling to emphasise curves bent to higher photon fluxes.

This can be explained by erroneous energy measurements due to pulse pile-up. Thereby, several photons featuring lower energies than the threshold reach the detector during its dead time. Consequently, their energies are added up and a single
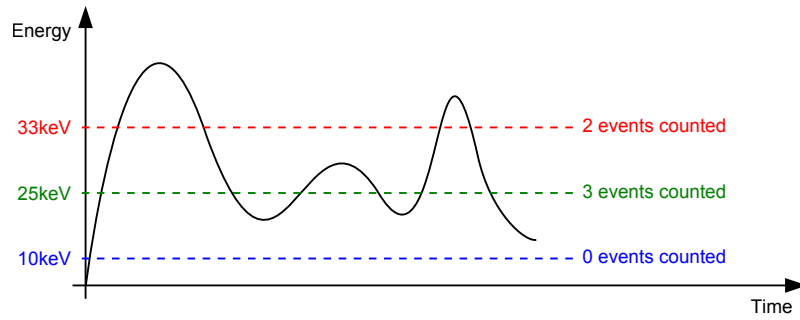
Figure 4.26: Influence of the energy threshold on the count rates.

event is counted.

If the energy threshold is set above the mean photon energy, the phenomenon of erroneous energy measurements will thus be more probable. At pulse pile-up, only the erroneous count rates but not the erroneous energy measurements are correctable (see section 2.2.2). Thus, according to the measurement results shown in figure 4.27, reconstructions at high photon fluxes for high energy thresholds are not possible with the applied detector. This statement could be verified by several control measurements, as illustrated below.

(a) 3 mA   **(b)** 40 mA   **(c)** 40 mA, corrected
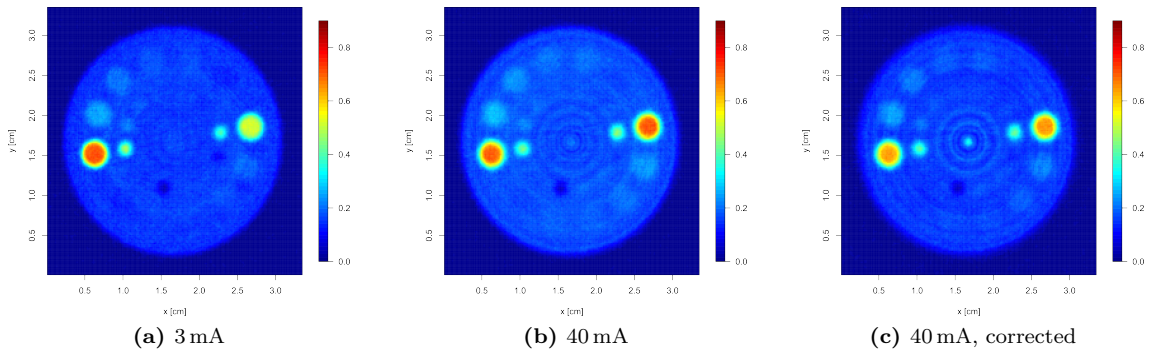
Figure 4.27: CT reconstructions at an energy threshold of 52 keV. All of the other settings are equal to figure 4.23. Due to an energy threshold above the mean photon energy of 44.5 keV it is not possible to reconstruct the CT images at high photon fluxes correctly.

To obtain images across a certain energy range (in this case four energy ranges), the projections are corrected for inhomogeneities and afterwards, the projection with the higher THL value is subtracted from the one with the lower threshold at the same projection angle. This algorithm leads to the low photon flux CT images, as illustrated in figure 4.28, and the high photon flux CT images, shown in figure 4.29. The 100th pixel row is used for the reconstructions since this detector row features only few non-counting pixels and there are only few bubbles in the phantom.

In the measurements obtained at a low photon flux, both K-edges, for iodine

(a) 25-32 keV

(b) 35-42 keV

(c) 42-49 keV

(d) 52-59 keV
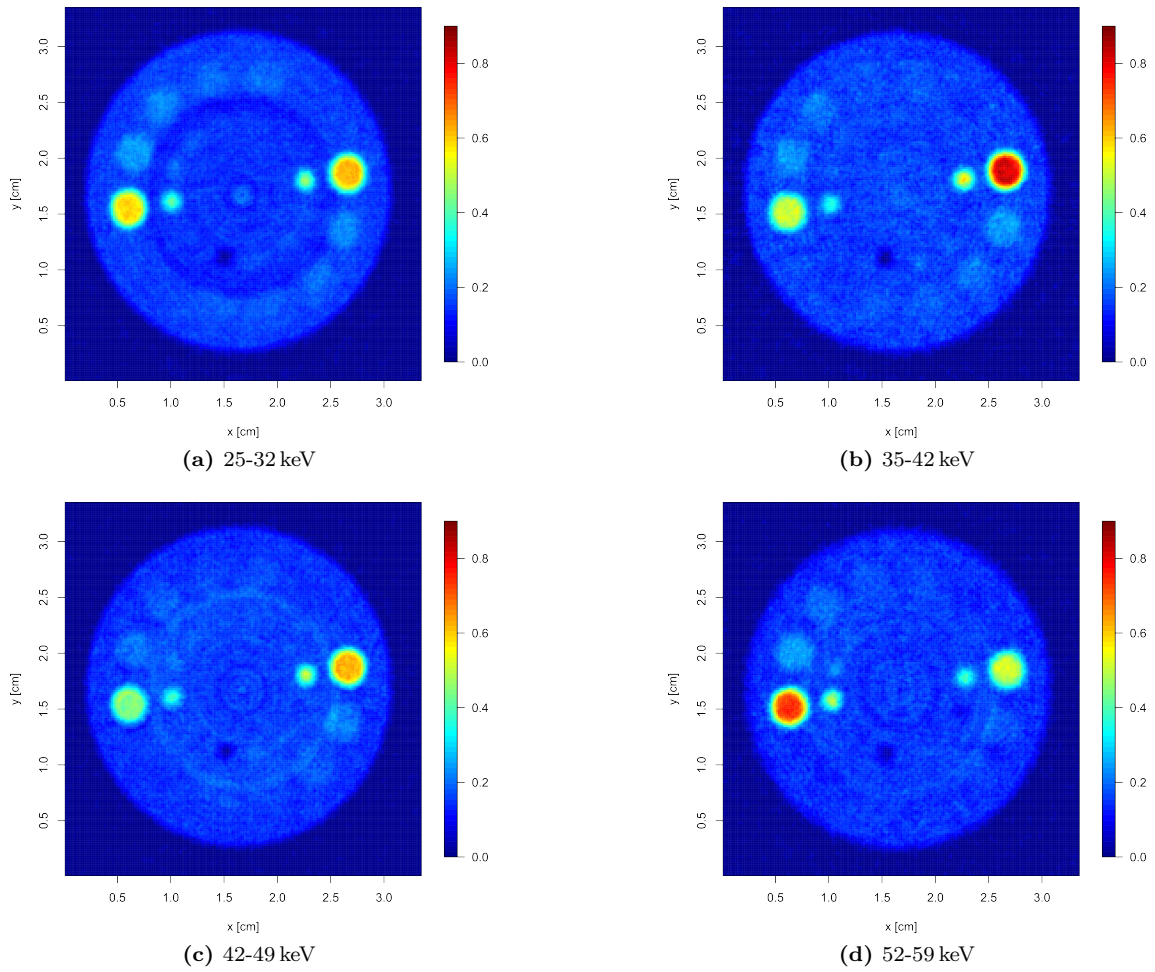
Figure 4.28: Cross-sectional CT images of the phantom at a low photon flux of $\Phi = 1.0 \cdot 10^6 \, \text{mm}^{-2}\text{s}^{-1}$ ($I_{\text{tube}} = 3 \, \text{mA}$) and different energy thresholds.

and gadolinium, are explicitly visible at the highest concentration. The absorption coefficient of iodine increases between the energy windows one and two ($33.2 \, \text{keV}$) and the absorption coefficient of gadolinium between the windows three and four ($50.2 \, \text{keV}$). These changes can be explained by the K-edges of the corresponding materials, as shown in figure 4.30. The K-edge is characteristic for a specific element and can be used for identification.

While both K-edges are explicitly visible in the measurements obtained at a low photon flux, only the K-edge of iodine can be weakly identified at a high flux.

Contrast to Noise Ratio (CNR)

A measure, which describes the image quality of the obtained CT reconstruction images, is the CNR, which is defined by equation 4.5. Here, μ_{rec} can be obtained by the mean of all reconstructed absorption coefficients in a quadratic area of a

(a) 25-32 keV

(b) 35-42 keV

(c) 42-49 keV

(d) 52-59 keV
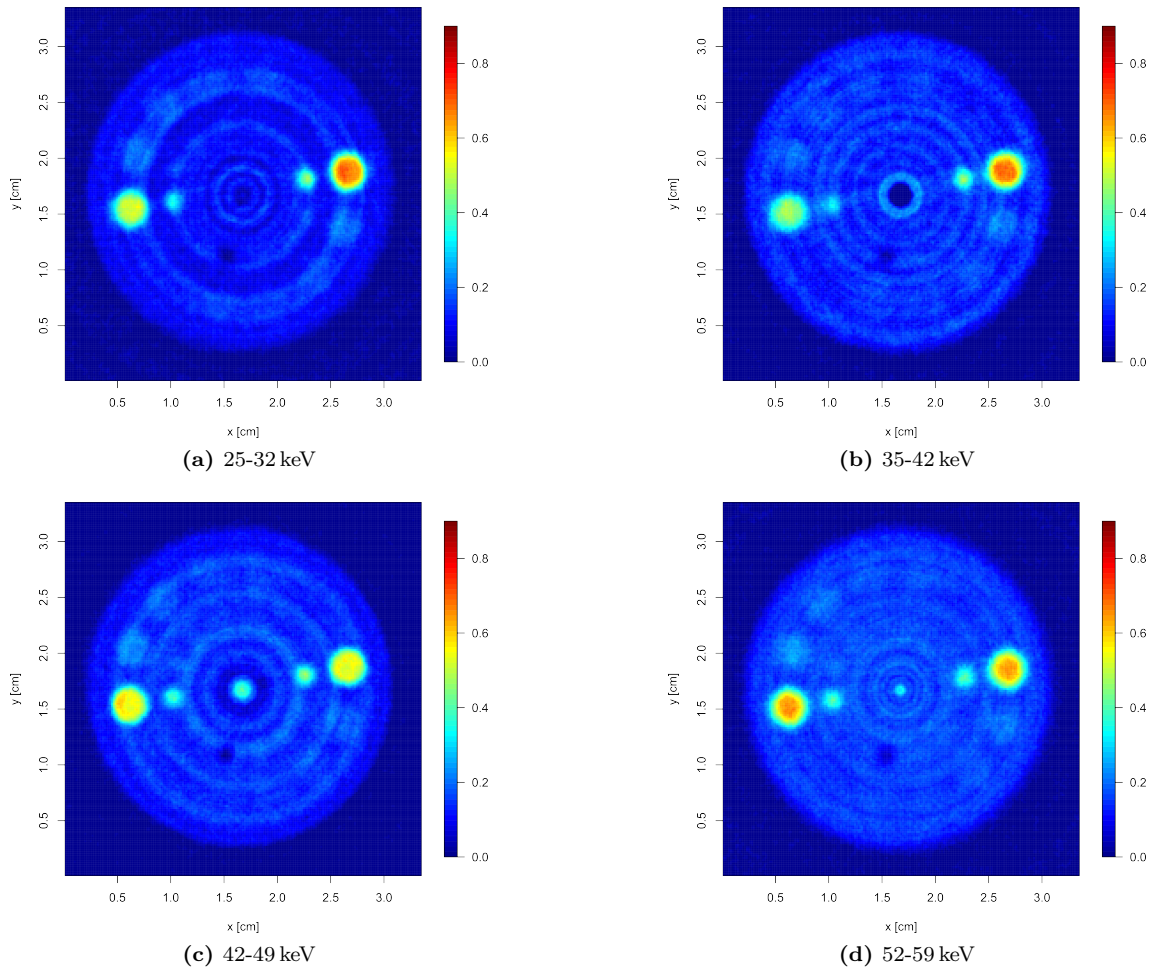
Figure 4.29: Cross-sectional CT images as in figure 4.28, but at a high photon flux of $\Phi = 1.3 \cdot 10^7 \, \text{mm}^{-2}\text{s}^{-1}$ ($I_{\text{tube}} = 40 \, \text{mA}$). Almost all spectroscopic information has been lost.

capillary and $\sigma_{\mu_{rec}}$ represents their standard deviation [Kalender, 2000].

$$CNR = \frac{\mid \mu_{rec}^{element} - \mu_{rec}^{PMMA} \mid}{\sqrt{\sigma_{\mu_{rec}^{element}}^2 + \sigma_{\mu_{rec}^{PMMA}}^2}} \tag{4.5}$$

The error is obtained by the standard error, shown in equation 4.6, where only the direct neighbouring CT slices are evaluated. Thus, it follows $N = 3$. The standard error is calculated by $\frac{1}{\sqrt{N}}$ times the standard deviation:

$$\Delta CNR = \sqrt{\frac{1}{N(N-1)} \sum_{i=1}^{N} (CNR_i - \overline{CNR})^2} \tag{4.6}$$
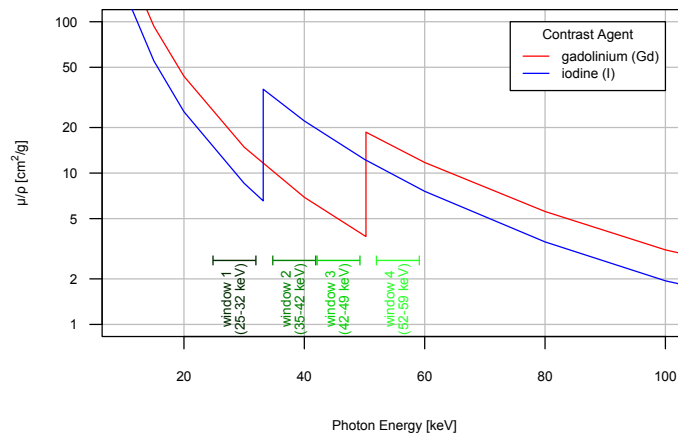
Figure 4.30: Mass attenuation coefficient versus photon energy for the applied contrast agents[19]. Whereas the K-edge of gadolinium is situated at 33.2 keV, the K-edge of iodine is at at 50.2 keV.
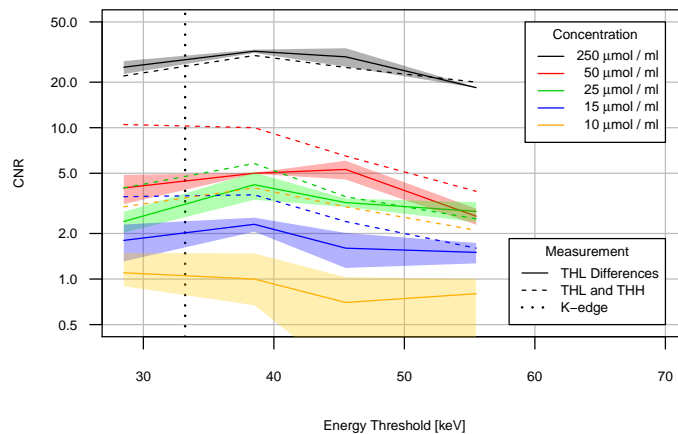
Figure 4.31: Results of the CNR for gadolinium at low photon flux and for the large capillaries. The CNR increases above the K-edge. The dashed lines indicate the results obtained by Schulze [2011], using the THL and THH DACs in contrast to calculating the differences of two measurements with different energy thresholds, as performed here. The coloured areas surrounding the curves illustrate the measurement errors. The CNR values on the y-axis are illustrated in logarithmic scale.

---

[19]mass attenuation coefficients obtained from the National Institute of Standards and Technology (NIST), XCOM: photon cross sections database [Online; accessed 20-October-2012]: http://www.nist.gov/pml/data/xcom/index.cfm

with $\overline{CNR} = \frac{1}{N} \sum_{i=1}^{N} CNR_i$.

The results of the measurements at a low photon flux at $3\,\mathrm{mA}$ are illustrated in figures 4.31 and 4.32.
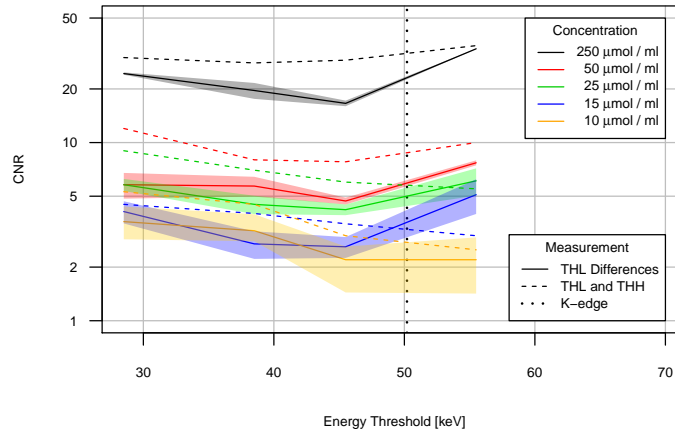
Figure 4.32: As in figure 4.31, but for gadolinium.

It can be seen, that the concentrations higher than $10\,\frac{\mu mol}{ml}$ of iodine are separable from PMMA. For gadolinium, all of the concentrations are verifiable. The K-edges
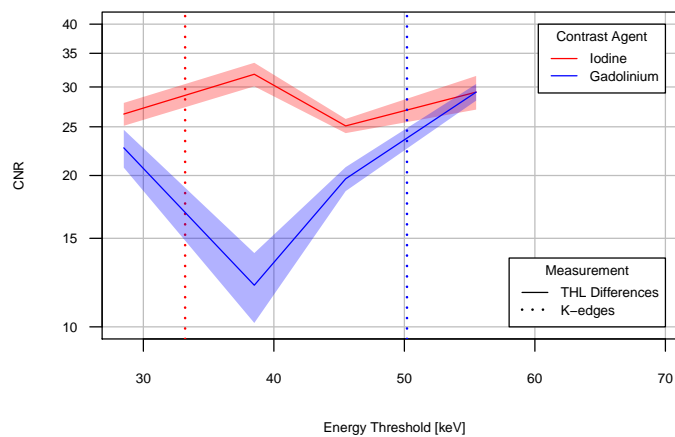
Figure 4.33: CNR for both contrast agents at high photon flux for the large capillaries and the highest concentration of $250\,\frac{\mu mol}{ml}$. The CNR slightly increases above the K-edge of iodine, but not so for gadolinium.

of iodine and gadolinium are visible down to a concentration of $15\,\frac{\mu mol}{ml}$, but they are more pronounced for gadolinium. At a concentration of $10\,\frac{\mu mol}{ml}$, the position of the capillaries could only be guessed for most of the reconstructions.

In comparison to the results obtained at a THL and THH energy threshold, all of the examined CNR values are lower, except for iodine at a concentration of $250\,\frac{\mu mol}{ml}$. This leads to the assumption that for low photon fluxes the method using both DACs is preferable. Nevertheless, the procedure in this thesis is chosen since less energy threshold drifts of the different detector chips are expected. The detector stability is a determining factor, especially at high photon fluxes.

In figure 4.33, the CNR for the high photon flux at $40\,\mathrm{mA}$ is illustrated only for the highest concentration of $250\,\frac{\mu mol}{ml}$ due to the increased presence of artefacts. While the K-edge of iodine is slightly visible between the first and second energy windows, the K-edge of gadolinium is not distinguishable due to the missing spectroscopic information of the photons at higher energy thresholds. The K-edge of iodine can be identified by just considering the first three energy windows.

5 Summary & Conclusion

In this master thesis, Medipix2 MXR photon counting detectors with pixel pitches of $110\,\mu m$ and $165\,\mu m$ were examined. The detectors studied feature $1\,mm$ thick CdTe sensors. The aim of this master thesis was to examine the saturation effects of the detectors at high photon fluxes.

It was shown that the maximum tolerable photon flux can be increased by optimised I_{Krum} settings at the cost of a degraded energy response function. For the pixel pitch of $165\,\mu m$ and an I_{Krum} value of 20, the deviation from an ideal linear response of more than $10\,\%$ was already reached at a critical photon flux of $4 \cdot 10^6\,mm^{-2}\,s^{-1}$. For an I_{Krum} value of 140, this value could be extended to $13 \cdot 10^6\,mm^{-2}\,s^{-1}$. While the I_{Krum} DAC influences the analog and the DelayN DAC the digital pile-up, a separation between different saturation effects could be shown. Thus, by setting the I_{Krum} and DelayN values to upper limits, the effect of sensor polarisation could be filtered.
Furthermore, increased I_{Krum} settings enable to compensate for higher leakage currents. In this way, the number of non-counting single pixels could be decreased and bulk defects, appearing as insensitive areas on images, could be reduced in size or completely removed.

With the aid of Monte Carlo simulations, the X-ray tube current was converted to universal photon fluxes. Additionally, it was possible to estimate the detrapping time in CdTe to be lower than $3.0 \cdot 10^{-2}\,s$ for $70\,kVp$.

After studying the behaviour of the photon counting detectors employed at high photon fluxes, CT imaging was performed. Therefor a phantom made of PMMA and filled with various concentrations of the contrast agents iodine and gadolinium was used. In order to obtain spectral resolution, projections at four different energy ranges, comprising the K-edges of the contrast agents, were acquired. Before CT reconstructions were performed, it was useful to correct the projections by different image processing algorithms. The advantages of higher photon fluxes are an increased photon throughput across the measured objects and a reduced acquisition time.
Furthermore, the following could be noted: Especially at high photon fluxes, image inhomogeneities influence the CT reconstruction. By means of the analysis of the detector's response at different photon fluxes, an algorithm was developed, which made it possible to correct these artefacts at low discriminator settings.
The K-edges for both contrast agents are visible for the low photon flux. For the high flux, at least the K-edge of iodine could be identified, since this edge is below

the mean applied photon energy. Additionally, side effects in form of erroneous energy signals due to pile-up effects did not occur severely, yet.

However, for future studies it would be interesting to determine if an increase of approximately the mean photon energy lead to advantages for the pile-up correction. In principle, the Medipix2 MXR detector should be operated in its linear range at low photon fluxes if the spectral information is important.

Bibliography

Antonuk, L. E., Jee, K.-W., El-Mohri, Y., Maolinbay, M., Nassif, S., Rong, X., Zhao, Q. and Siewerdsen, J. [2000], 'Strategies to improve the signal and noise performance of active matrix, flat-panel imagers for diagnostic x-ray applications', *Med. Phys.* **27**(2), 289.

Bale, D. and Szeles, C. [2008], 'Nature of polarization in wide-bandgap semiconductor detectors under high-flux irradiation: Application to semi-insulating Cd(1-x)Zn(x)Te', *Phys. Rev. B* **77**(3), 35205.

Ballabriga, R., Campbell, M., Heijne, E. H. M., Llopart, X. and Tlustos, L. [2007], 'The medipix3 prototype, a pixel readout chip working in single photon counting mode with improved spectrometric performance', **6**, 3557–3561.

Campbell, M., Heijne, E., Meddeler, G., Pernigotti, E. and Snoeys, W. [1998], 'Readout for a 64 x 64 pixel matrix with 15-bit single photon counting', *IEEE Trans. Nucl. Sci.* **45**(3), 751–753.

Funaki, M., Ozaki, T., Satoh, K. and Ohno, R. [1999], 'Growth and characterization of CdTe single crystals for radiation detectors', *Nucl. Instr. and Meth. in Phys. Res. A* **436**(1-2), 120–126.

Greiffenberg, D. [2010], 'Charakterisierung von CdTe-medipix2-pixeldetektoren', PhD thesis, University of Freiburg, Germany. [Online; accessed 20-October-2012].
URL: `http://www.freidok.uni-freiburg.de/volltexte/7854/pdf/Dissertation_Greiffenberg.pdf`

Holy, T., Jakubek, J., Pospisil, S., Uher, J., Vavrik, D. and Vykydal, Z. [2006], 'Data acquisition and processing software package for medipix2', *Nucl. Instr. and Meth. A* **563**(1), 254–258.

Hunklinger, S. [2009], *Festkörperphysik*, 2nd edn, Oldenbourg.

Jähne, B. [2005], *Digitale Bildverarbeitung*, 6th edn, Springer.

Kak, A. C. and Slaney, M. [2001], *Principles of Computerized Tomographic Imaging*, Society for Industrial Mathematics.

Kalender, W. [2000], *Computertomographie*, 1st edn, Publicis MCD.

Kane, P., Kissel, L., Pratt, R. and Roy, S. [1986], 'Elastic scattering of gamma-rays and x-rays by atoms', *Phys. Rep.* **140**(2), 75–159.

Kawkarow, I. [2000], 'Accurate condensed history monte carlo simulation of electron transport. I. EGSnrc, the new EGS4 version', *Med. Phys.* **27**, 485.

Kawkarow, I. [2004], 'Large efficiency improvements in beamnrc using directional bremsstrahlung splitting', *Med. Phys.* **31**, 2883.

Koenig, T. [2011 a], 'Exploring coherent phenomena and energy discrimination in x-ray imaging', PhD thesis, University of Heidelberg, Germany. [Online; accessed 20-October-2012].
URL: `http://www.ub.uni-heidelberg.de/archiv/11933`

Koenig, T., Schulze, J., Zuber, M., Rink, K., Butzer, J., Hamann, E., Cecilia, A., Zwerger, A., Fauler, A., Fiederle, M. and Oelfke, U. [2012], 'Imaging properties of small-pixel spectroscopic x-ray detectors based on cadmium telluride sensors', *Phys. Med. Biol.* **57**, 6743–6759.

Koenig, T., Zuber, M., Zwerger, A., Schuenke, P., Nill, S., Fauler, A., Fiederle, M. and Oelfke, U. [2011 b], 'A comparison of various strategies to equalize the lower energy thresholds of a CdTe medipix2 hexa detector for x-ray imaging applications', *J. Inst.* **6**(01), C01074.

Koenig, T., Zwerger, A., Zuber, M., Schuenke, P., Nill, S., Guni, E., Fauler, A., Fiederle, M. and Oelfke, U. [2011 c], 'On the energy response function of a CdTe medipix2 hexa detector', *Nucl. Instr. and Meth. A* **648, Supplement 1**, S265–S268.

Kraus, V., Holik, M., Jakubek, J., Kroupa, M., Soukup, P. and Vykydal, Z. [2011], 'FITPix – fast interface for timepix pixel detectors', *J. Inst.* **6**(01), C01079.

Krummenacher, F. [1991], 'Pixel detectors with local intelligence: an IC designer point of view', *Nucl. Instr. and Meth. in Phys. Res. A* **305**, 527–532.

Llopart, X. [2007], 'Design and characterization of 64K pixels chips working in single photon processing mode', PhD thesis, Mid Sweden University. [Online; accessed 20-October-2012].
URL: `http://www.dissertations.se/dissertation/5efeeb398f/`

Llopart, X., Ballabriga, R., Campbell, M., Tlustos, L. and Wong, W. [2007], 'Timepix, a 65k programmable pixel readout chip for arrival time, energy and/or photon counting measurements', *Nucl. Instr. and Meth. A* **581**(1-2), 485–494.

Llopart, X., Campbell, M., Dinapoli, R., San Segundo, D. and Pernigotti, E. [2002], 'Medipix2: A 64-k pixel readout chip with 55-µm square elements working in single photon counting mode', *IEEE Trans. Nucl. Sci.* **49**(5), 2279.

Mertins, H.-C. and Gilbert, M. [2006], *Prüfungstrainer Experimentalphysik*, Elsevier.

Quan, E. [2009], 'Imaging properties of a rotation-free, arrayed-source micro-computed tomography system', PhD thesis, North Carolina State University, USA.

Rink, K., Koenig, T., Zuber, M., Zwerger, A., Fauler, A., Fiederle, M. and Oelfke, U. [2012], 'Saturation effects of CdTe photon counting detectors under high photon fluxes', *J. Inst.* **accepted**.

Salvat, F., Fernandez-Varea, J. M., Acosta, E. and Sempau, J. [2001], 'PENELOPE: a code system for monte carlo simulation of electron and photon transport'. [Online; accessed 20-October-2012].
URL: `http://www.nea.fr/dbprog/penelope.pdf`

Schlegel, W. and Bille, J. [2002], *Medizinische Physik 2: Medizinische Strahlenphysik*, 1st edn, Springer Berlin Heidelberg.

Schlomka, J. P., Roessl, E., Dorscheid, R., Dill, S., Martens, G., Istel, T., Bäumer, C., Herrmann, C., Steadman, R., Zeitler, G., Livne, A. and Proksa, R. [2008], 'Experimental feasibility of multi-energy photon-counting k-edge imaging in preclinical computed tomography', *Phys. Med. Biol.* **53**, 4031–4047.

Schuebel, A. [2012], 'Analysis and Control of Threshold Instabilities in Medipix2 MXR Detectors', bachelor thesis, University of Heidelberg, Germany.

Schulze, J. [2011], 'Spectral Computed Tomography with Photon Counting Medipix2 MXR Detectors and CdTe Sensors', diploma thesis, University of Heidelberg, Germany.

Shikhaliev, P. M. [2008], 'Energy-resolved computed tomography: first experimental results', *Phys. Med. Biol.* **53**, 5595–613.

Shikhaliev, P. M. and Fritz, S. G. [2011], 'Photon counting spectral ct versus conventional ct: comparative evaluation for breast imaging application', *Phys. Med. Biol.* **56**, 1905–1930.

Shikhaliev, P. M., Fritz, S. G. and Chapman, J. W. [2009], 'Photon counting multi-energy x-ray imaging: effect of the characteristic x rays on detector performance', *Med. Phys.* **36**, 5107.

Spieler, H. [2006], *Semiconductor Detector Systems*, Oxford University Press.

Tlustos, L. [2005], 'Performance and limitations of high granularity single-photon processing X-ray imaging detectors', PhD thesis, Vienna University of Technology, Austria. [Online; accessed 20-October-2012].
URL: `http://cdsweb.cern.ch/record/846447/files/thesis-2005-032.pdf`

Zuber, M. [2010], 'Threshold Equalisation of a Medipix2 MXR Hexa Detector', bachelor thesis, University of Heidelberg, Germany.

Zuber, M. [2012], 'Investigating the Energy Response of Small-Pixel Spectroscopic X-Ray Detectors', master thesis, University of Heidelberg, Germany.

List of Figures

List of Tables

List of Acronyms

3D	three dimensional
ADC	analog-to-digital converter
$_{13}$Al	aluminium
$_{95}$Am	americium
$_{47}$Ag	silver
ASIC	application-specific integrated circuit
$_6$C	carbon
CCD	charge-coupled device
$_{48}$Cd	cadmium
CdTe	cadmium telluride
CERN	European Organization for Nuclear Research
CMOS	complementary metal oxide semiconductor
CT	computed tomography
$_{29}$Cu	copper
DAC	digital-to-analog converter
DKFZ	German Cancer Research Center
EGS	electron gamma shower
ENC	equivalent noise charge
FMF	Freiburg Materials Research Center
GaAs	gallium arsenide
$_{64}$Gd	gadolinium
HU	Hounsfield units
$_{53}$I	iodine
IPCT	inter-pixel cross-talk
iWoRID	International Workshop on Radiation Imaging Detectors
KIT	Karlsruher Institut für Technologie
LHC	large hadron collider
$_{42}$Mo	molybdenum
MRI	magnetic resonance imaging
MV	mega-voltage
PMMA	polymethyl methacrylate
$_{14}$Si	silicon
SNR	signal-to-noise ratio
$_{52}$Te	tellurium
THL	low energy threshold
THH	high energy threshold
ToT	time over threshold
$_{74}$W	tungsten

Acknowledgements

Declaration

Ich versichere, dass ich diese Arbeit selbstständig verfasst und keine anderen als die angegebenen Quellen und Hilfsmittel benutzt habe.

Heidelberg, den 01. Dezember 2012   ....